

# Discovery of cellular substrates of human RNA decapping enzyme Dcp2 using a stapled bicyclic peptide inhibitor

Yang Luo<sup>†‡</sup>, Jeremy A. Schofield<sup>‡</sup>, Zhenkun Na<sup>†‡</sup>, Tanja Hann<sup>†</sup>, Matthew D. Simon<sup>‡</sup> and Sarah A. Slavoff<sup>†‡¶\*</sup>

<sup>†</sup>Department of Chemistry, Yale University, New Haven, Connecticut 06520, United States

<sup>‡</sup>Chemical Biology Institute, Yale University, West Haven, Connecticut 06516, United States

<sup>¶</sup>Department of Molecular Biophysics and Biochemistry, Yale University, New Haven, Connecticut 06529, United States

<sup>§</sup>Yale Combined Program in the Biological and Biomedical Sciences, Yale University, New Haven, Connecticut 06520, United States

\*Correspondence: [sarah.slavoff@yale.edu](mailto:sarah.slavoff@yale.edu)

THIS PDF FILE INCLUDES:

Main Text

Figure 1 to 7

Figure S1 to S6

Table S1

---

**SUMMARY:** Dcp2 is an RNA decapping enzyme that controls the stability of human RNAs that encode factors functioning in transcription and the immune response. While >1800 human Dcp2 substrates have been identified, compensatory expression changes secondary to genetic ablation of *Dcp2* have complicated a complete mapping of its regulome. Cell-permeable, selective chemical inhibitors of Dcp2 could provide a powerful tool to study Dcp2 specificity. Here, we report phage display selection of CP21, a bicyclic peptide ligand to Dcp2. CP21 has high affinity and selectivity for Dcp2 and inhibits Dcp2 decapping activity toward selected RNA substrates in human cells. CP21 increases formation of P-bodies, liquid condensates enriched in intermediates of RNA decay, in a manner that resembles the deletion or mutation of Dcp2. We used CP21 to identify 76 previously undiscovered Dcp2 substrates. This work provides a first demonstration that Dcp2 inhibition can provide new insights into RNA decay.

---

KEYWORDS:

Dcp2; Chemical Genetics; RNA Decay; Cyclic Peptide; P-bodies

## INTRODUCTION

Regulated RNA degradation is an important step in control of gene expression. While much effort has been focused on understanding synthesis and processing of RNAs, we know substantially less about the pathways that control programmed RNA decay. The first step of 5'-to-3' exonucleolytic RNA decay, one of the major pathways that regulates the stability of the cytoplasmic transcriptome in eukaryotic cells, is the removal of the 7-methylguanosine (m<sup>7</sup>G) cap of deadenylated RNAs (Li and Kiledjian, 2010). In yeast this is primarily accomplished by the Nudix family decapping enzyme Dcp2 (Behm-Ansmant et al., 2006; Dunkley and Parker, 1999; Lykke-Andersen, 2002; Wang et al., 2002; Xu et al., 2006). This enzyme is subject to temporal and spatial regulation by coactivator proteins including Dcp1 (Li and Kiledjian, 2010), post-translational modifications (Yoon et al., 2010), and phase separation into membraneless organelles known as processing bodies (P-bodies) (Luo et al., 2018; Mugridge et al., 2018a). The landscape of RNA decapping enzymes is more complex in mammals than in lower eukaryotes (Grudzien-Nogalska and Kiledjian, 2017; Kiledjian, 2018). Mammals encode multiple Nudix family RNA decapping enzymes with distinct activities. Dcp2, Nudt16 (Li et al., 2011; Song et al., 2010) and Nudt3 (Grudzien-Nogalska et al., 2016) hydrolyze m<sup>7</sup>G caps, while Dxo/Rai1 hydrolyzes both unmethylated (Chang et al., 2012; Jiao et al., 2013) and NAD caps (Grudzien-Nogalska and Kiledjian, 2017; Jiao et al., 2017). The Nudix m<sup>7</sup>G hydrolases have the potential to regulate different target transcripts despite their lack of apparent *in vitro* sequence specificity (Song et al., 2010). While

evidence for orthogonal regulation of specific genes by Dcp2, Nudt16 and Nudt3 supports this hypothesis (Cohen et al., 2005; Grudzien-Nogalska et al., 2016; Li et al., 2011; Li et al., 2008), a complete mapping of the RNA substrates of m<sup>7</sup>G decapping enzymes in mammalian cells has not yet been achieved.

Dcp2 controls the stability of a large but specific subset of human transcripts. We recently obtained global, time-resolved measurements of RNA dynamics to identify ~1800 transcripts that are stabilized in *DCP2* knockout (KO) cells, suggesting that they are Dcp2 substrates (Luo et al., 2020). This and related studies have established that transcripts comprising the Dcp2 regulome are (1) enriched in P-bodies, (2) often modified with N<sup>6</sup>-methyladenosine (m<sup>6</sup>A), and (3) more likely to encode regulatory and immune-related factors (Li et al., 2012; Song et al., 2010; Wang et al., 2014). We also observed a significant number of destabilized RNAs and transcriptional changes in *DCP2* KO cells, indicative of secondary effects as a result of genetic compensation for *DCP2* deletion, thereby limiting comprehensive identification of Dcp2 targets. We reasoned that the development of a specific Dcp2 inhibitor would allow acute shut down of Dcp2 activity, thereby permitting mapping of Dcp2 substrates for which changes in decay rate are masked by secondary effects in *DCP2* KO.

Structural characterization of Dcp2-containing complexes in yeast has revealed the mechanistic basis for catalysis and allosteric activation (Figure 1a, left) (Charenton et al., 2016; Mugridge et al., 2018b; Mugridge et al., 2016; Paquette et al., 2018; Valkov et al., 2016; Wurm et al., 2017). Dcp2 uses a bipartite active site, with critical residues contributed both by the Nudix catalytic domain (CD) and the distal N-terminal regulatory domain (NRD). Yeast Dcp1/human DCP1A is a conserved activator of decapping, which contacts the Dcp2 NRD either through direct interaction with the Dcp1 EVH1 (Ena/VASP homology 1) domain in yeast (She et al., 2008) or through the scaffold protein EDC4 in higher eukaryotes (Chang et al., 2014; Tritschler et al., 2009) to promote formation of a pre-catalytic closed conformation of Dcp2. Additional factors, such as yeast Edc1 (Mugridge et al., 2018b; Valkov et al., 2016; Wurm et al., 2017) and Edc3 (Paquette et al., 2018), release autoinhibition by a C-terminal Dcp2 segment and correctly position residues critical for cap recognition and hydrolysis by Dcp2 in its active conformation. It is important to note that molecular details that regulate Dcp2 activity in human may be fundamentally different from yeast, especially with regard to reprogramming of protein-protein interaction networks (Figure 1a, right) (Chang et al., 2014; Chang et al., 2019; Na et al., 2020). Given the conformational flexibility and coactivator requirements of Dcp2, directly targeting the catalytic site with small-molecule inhibitors is likely to be challenging (Ziemniak et al., 2016). Furthermore, Dcp2 has low affinity for most small molecule cap analogs, requiring an intact, capped RNA substrate of at least 12 residues (Arribas-Layton et al., 2013), complicating *in vitro* screening.

Despite these challenges, Dcp2 inhibitors have been reported. These bivalent cap analogues, consisting of two m<sup>7</sup>G moieties joined by a 5'-to-5' tetraphosphate bridge to increase binding affinity, can bind to and inhibit the active conformation of Dcp2 at the catalytic site (Mugridge et al., 2016; Ziemniak et al., 2016). The D3 diastereomer of the most potent analog, bearing  $\alpha$ - and  $\delta$ -phosphorothiolate substitution, exhibited a K<sub>i</sub> of 121±16  $\mu$ M for *Schizosaccharomyces pombe* Dcp2 (spDcp2) (Ziemniak et al., 2016). These inhibitors exhibit increased affinity toward the reconstituted spDcp1/2 complex compared to spDcp2 alone, suggesting that they bind to the active conformation and making them particularly valuable for structural and mechanistic studies (Mugridge et al., 2018b; Mugridge et al., 2016). Nonetheless, these dinucleotide cap analogues may be poorly suited for use in determining the RNA substrates of Dcp2 in cells because of (1) membrane impermeability, (2) limited binding affinity and (3) possible lack of specificity for Dcp2 by binding only the Nudix domain.

To develop new inhibitors of Dcp2, one major challenge is the absence of a preformed, high affinity substrate binding pocket in Dcp2 for ligand or inhibitor binding. To address this challenge, we employed a strategy that could target surface or allosteric sites using proteomimetics (Horne and Grossmann, 2020). Chemically stapled or cyclized peptides are emergent classes of ligands developed to target large protein surfaces inaccessible by small molecules (Deyle et al., 2017; Vinogradov et al., 2019; Walensky and Bird, 2014). In addition to mimicking structured protein-binding domains, these molecules feature resistance to proteolytic degradation compared to their linear equivalents *in vivo*, and can display detectable membrane permeability (Dietrich et al., 2017; LaRochelle et al., 2015). We were particularly inspired by work from Heinis *et al.*, which reported a phage-encoded stapled bicyclic peptide library that has enabled successful *in vitro* selection of ligands for various protein targets (Heinis et al., 2009). This class of stapled peptides have been demonstrated to form interaction surfaces of approximately 700 Å<sup>2</sup> and are more conformationally restricted than their monocyclic counterparts, which make them ideal for binding flat surfaces and protein-protein interaction interfaces (Angelini et al., 2012; Vinogradov et al., 2019). Here, we applied this approach to identify a cyclic peptide, CP21, which functions as a selective and cell-permeable human Dcp2 ligand. We demonstrate that CP21 increases the stability of specific Dcp2 target RNAs and the formation of P-bodies, likely through indirect depletion of DDX6 and associated RNAs from the Dcp2 decapping complex. We use this molecule to identify 76 Dcp2 substrates invisible to previous studies based on genetic ablation of *DCP2* in mammals (Luo et al., 2020; Song et al., 2010). Together, our data illustrates the utility of macrocyclic ligands in the biochemical characterization and substrate identification of human Dcp2, establishing this approach as an attractive platform to study the biology of RNA decay enzymes.

## RESULTS

### Phage display screening identifies CP21 as a ligand of human Dcp2

We hypothesized that chemically stapled bicyclic peptides might achieve specificity for binding Dcp2 through interactions with one or more large surfaces on the protein, as previously reported for human urokinase-type plasminogen activator (uPA) (Angelini et al., 2012). We used a previously reported initial peptide library that consisted of two fully

randomized 6-mer peptide sequences flanked by a total of three cysteine residues displayed on a disulfide-free phage pIII protein, then chemically cyclized with 1,3,5-tris(bromomethyl)benzene (TBMB) (Rentero Rebollo and Heinis, 2013) (Figure 1b). We immobilized Dcp2 with a site-specific biotinylation strategy (Fairhead and Howarth, 2015; Howarth et al., 2005) to avoid blocking important surfaces of the enzyme, as might occur using less directed chemistry. We appended a 15-amino acid BirA biotin ligase substrate, AviTag peptide (Schatz, 1993), to the C-terminus of full-length Dcp2 (Dcp2<sup>FL</sup>-AP), and the tagged protein was labeled *in vitro* using purified BirA and biotin. Successful biotinylation was confirmed using streptavidin enrichment (Figure S1a-c). Biotinylated Dcp2<sup>FL</sup>-AP was immobilized on streptavidin beads for phage display selection. Starting with 10<sup>10</sup> purified TBMB-modified phage particles, three rounds of selection were performed, including amplification of enriched phage and chemical cyclization of the displayed sequences before each round of selection. To facilitate enrichment of high-affinity Dcp2 binders, the stringency of selection was increased in the 2<sup>nd</sup> and the 3<sup>rd</sup> round by doubling the number of wash steps and decreasing the amount of immobilized Dcp2<sup>FL</sup>-AP. A beads-only negative control was included in all steps to identify non-specific streptavidin binders. One hundred colonies were sequenced from the last round of selection, and we identified two classes of sequences (Figure 1c): the first class was enriched in positively charged or polar amino acids and proline; the second class, which we did not pursue farther given the high likelihood that these members displayed peptides prone to aggregation and/or nonspecific binding, was characterized by highly hydrophobic and aromatic residues. Further considering sequence consensus in the first class (Figure 1c, top), we observed that proline was strongly preferred in position 1 of the first loop, and enriched in position 1 of the second loop as well as positions 5 or 6 of both loops. Enrichment of positively charged or uncharged polar amino acids was observed in position 3 (K, H or Q) and position 4 (H) of loop 1. Weaker convergence was observed in loop 2. New affinity maturation libraries were then constructed to recapture the convergence in the first class by fixing proline in the first and either the fifth or the sixth position of loop 1, together with a histidine or a glutamine at the fourth position of loop 1. The remaining positions were randomized. These libraries were mixed and panned using stringent conditions (40 to 10 pmol of Dcp2<sup>FL</sup>-AP). Sequencing clones from the enriched library revealed emergence of a new, albeit weak, consensus with preference for proline at position 3 of loop 2 flanked by positively charged residues (Figure 1d). Representative sequences from this selection were chosen for further characterization.

#### CP21 interacts with Dcp2 *in vitro*

To identify an optimal Dcp2 ligand from the enriched sequences, we screened individual clones using an orthogonal *in vitro* binding assay. The DNA sequences of enriched peptides from both primary selection and affinity maturation were expressed, purified and TBMB-cyclized as peptide-D1D2-FLAG (D1D2, disulfide-free phage protein pIII domain) fusions to test their interaction with GST-Dcp2<sup>FL</sup> (Figure S1b,d). The top hit, CP21 (Figure 2a), arose from affinity maturation, and its D1D2 fusion showed 15-fold higher enrichment by Dcp2 compared to the control (unfused D1D2 phage protein) in this assay (Figure 2b). We then chemically synthesized and cyclized CP21 containing the same core 6×6 sequence with an extra N-terminal alanine and C-terminal amidated glycine appended, in accordance with prior reports (Heinis et al., 2009). This synthetic peptide construct was utilized for all subsequent experiments and hereafter is indicated by the term CP21 (Figure 2a and Figure S2a). The  $K_D$  of CP21 for the catalytically active Dcp2<sup>1-349</sup> truncation construct (Piccirillo et al., 2003) (Figure S1a,b) was  $116 \pm 31$  nM by isothermal titration calorimetry (ITC) (Figure 2c), while its affinity for another cytoplasmic decapping enzyme, full-length human Nudt16, was approximately 300-fold lower ( $K_D = 34.5 \pm 1$   $\mu$ M) (Figure 2d). Additionally, the synthetic all-D enantiomeric form of CP21 (D-CP21, Figure S2b) showed undetectable binding to Dcp2<sup>1-349</sup> in ITC (Figure 2e), demonstrating that the 3-dimensional orientation of the sidechains, rather than the general biophysical properties of the peptide, was responsible for binding. These results support our conclusion that CP21 binds specifically to Dcp2.

#### CP21 binding requires a C-terminal disordered segment of Dcp2

To map the Dcp2 interface responsible for CP21 binding, we used photo-cross-linking-based affinity enrichment and proteomics. To make a CP21 analogue with a photo-crosslinker that retains binding, we replaced residues that were not conserved in the most enriched peptide sequences from the phage display selection with photoreactive amino acids, L-Photo-Methionine (Photo-M) or L-Photo-Leucine (Photo-L), in loops or near the cyclization center (Photo-CP-1 to -3, Figure S2c-e and Figure S3a). Biotin was added to the N-terminus of all peptides through an alkyl linker as an affinity handle for enrichment of crosslinked proteins. Reaction with Photo-CP-3 led to the greatest enrichment of purified Dcp2<sup>1-349</sup> over background (Figure S3b). To confirm that Photo-CP-3 engages Dcp2 at the same site as CP21, we performed a competitive pulldown assay and observed that increasing concentration of Photo-CP-3 effectively decreased FLAG-tagged CP21-D1D2 binding to Dcp2 (Figure S3c). We concluded that Photo-CP-3 competes with CP21 for Dcp2 binding. We then performed mass spectrometry analysis of pre- and post-Photo-CP-3-cross-linked Dcp2<sup>1-349</sup> to identify its binding site(s) (Figure S3d). Three candidate sites of interaction were found at or near the Nudix domain, and one more was found near the C-terminal FEB (phenylalanine-rich EDC4 binding) motif known to interact with EDC4, an important scaffolding protein of the active human decapping complex (Chang et al., 2014; Chang et al., 2019). This unexpected C-terminal candidate led us to more closely examine the functional relevance of binding to the disordered C-terminal region of Dcp2.

We hypothesized that the disordered C-terminal region may be involved in Dcp2 activity or protein interactions, which may be disrupted by CP21 binding. Recent structural studies of yeast Dcp2 demonstrated the importance of intrinsically disordered regions in regulatory autoinhibition (Paquette et al., 2018), but the C-terminus of human Dcp2 is distinct in sequence from that of yeast and has not been characterized beyond the FEB motif. We therefore examined the interaction of CP21 with

the Dcp2 C-terminus. We generated alanine mutants of GST-tagged Dcp2<sup>FL</sup> between amino acids 325 and 333 and examined binding with CP21-D1D2-FLAG containing the candidate interaction site for CP21 (Figure S3c, blue). Q332A or K333A mutations had the largest effect on binding, leading to ~50% reduction in the amount of CP21 fusion enriched by the pull-down compared to wild-type Dcp2 (Figure S3e). We therefore hypothesized that CP21 could remodel protein-protein interactions within the decapping complex. Intriguingly, we observed depletion of DDX6 from the decapping complex immunoprecipitated from CP21 vs D-CP21 treated HEK293T cells (Figure S4). However, DDX6 does not directly contact Dcp2 and was shown instead to interact with the human decapping machinery via EDC3 (Jonas and Izaurralde, 2013). It is hence possible that CP21 affects recruitment of DDX6 and/or its bound RNAs indirectly. Together, these data suggest that CP21 engages with a disordered C-terminal region of Dcp2 as well as the Nudix domain and decreases DDX6 association with the decapping complex.

#### CP21 specifically binds to Dcp2 in cells

To investigate the ability of CP21 to engage Dcp2 in the presence of other cellular proteins, we used Photo-CP-3 to examine direct binding of CP21 to Dcp2 in whole cell lysates (Figure 3a). We incubated Photo-CP-3 with HEK293T cell lysates over-expressing Dcp2 and compared enrichment in the presence or absence of 5-fold excess of unlabeled competitor CP21 ([CP21<sub>unlabeled</sub>] = 300  $\mu$ M). Quantitative proteomics revealed enrichment of Dcp2, supporting the ability of CP21 to directly bind over-expressed Dcp2 in the cellular context (Figure 3b); however, we note that Dcp2 over-expression limits conclusions regarding the selectivity of CP21 for Dcp2 in cells.

Cyclized peptides can be somewhat cell permeable compared to their linear counterparts (Chu et al., 2015; Dietrich et al., 2017). We therefore asked whether CP21 could penetrate the cell membrane. N-terminally FITC-labeled CP21 with an aminohexanoic (Ahx) acid spacer was chemically synthesized, purified (Figure S2f, g), and its cellular uptake examined by live-cell fluorescence confocal microscopy. HEK293T cells incubated with FITC-Ahx-CP21 or the all-D enantiomer (3  $\mu$ M, 5 h) exhibited comparable weak internalization, based on a low level of diffuse cytoplasmic signal (Figure 3c).

To evaluate Dcp2-CP21 interaction in the cytoplasm, a cellular thermal shift assay (CETSA) was performed in HEK293T cells (Jafari et al., 2014). In comparison to the vehicle-treated group, the melting temperature of cellular Dcp2 was increased by 3.2  $^{\circ}$ C when cells were treated with 2  $\mu$ M CP21, while no significant difference was observed when cells were treated with D-CP21 (Figure 3d). This observation is consistent with CP21-Dcp2 interaction in cells. In contrast, the melting temperature of COPA, a potential off-target enriched by cross-linking to Photo-CP-3, was not significantly changed by CP21 treatment compared to vehicle, while D-CP21 treatment decreased the melting temperature by 1  $^{\circ}$ C (Figure S5a). Intriguingly, DDX6 displayed a significant 2.5  $^{\circ}$ C drop in melting temperature with CP21 treatment, compared to the vehicle or D-CP21 (Figure S5b). Stabilities of two direct binding partners of DDX6 that contact Dcp2, DCP1A and EDC3, were not altered by CP21 compared to controls (Figure S5c,d), indicating that the destabilization of DDX6 is specific. The observed destabilization of DDX6 is consistent with its lower association with the immunoprecipitated decapping complex resulting in a loss of stabilizing protein-protein interactions (Dai et al., 2018; Tan et al., 2018). Together with selective cross-linking of Photo-CP-3 to Dcp2 in lysates, these results are again consistent with a model in which CP21 binds directly to Dcp2 in cells, which leads to depletion of DDX6 from the decapping complex, likely via an indirect mechanism.

#### CP21 inhibits Dcp2 in cells

Because CP21 was selected as a Dcp2 ligand, it was unclear whether CP21 could inhibit Dcp2. We therefore investigated the specificity and functional consequence of CP21 toward Dcp2 activity inside cells by measuring the transcript levels of known Dcp2 substrates RNAs using qRT-PCR. Previously, Kiledjian and coworkers reported the *RRP41* RNA as a preferred substrate of human Dcp2 (Li et al., 2008). More recently, we demonstrated that *HOXA13* RNA is a Dcp2 target (Luo et al., 2020). We thus used these two transcripts as endogenous reporters to evaluate the effect of cellular CP21 delivery on Dcp2 activity. Briefly, cells were pre-treated with compounds, then transcription was inhibited with actinomycin D and RNA levels assessed at specified timepoints to measure decay. Both Dcp2 substrate RNAs were significantly stabilized by CP21 (2  $\mu$ M) compared to controls (vehicle or D-CP21) (Figure 4a). The fact that D-CP21 did not alter the stability of any tested RNAs indicates that the observed inhibition of RNA decay was specific to inhibitory activity of CP21 in its all-L form. Importantly, we found that CP21 did not lead to a further increase in the stability of the *RRP41* transcript in the *DCP2* KO cell line, suggesting that CP21 mediates its *RRP41*-stabilizing effect specifically through Dcp2 and not via off-target inhibition or other non-specific effects (Figure 4b). Stability of a non-Dcp2 substrate RNA, *PLBD2* (Luo et al., 2020), remained unchanged by CP21 treatment (Figure 4c), further supporting a specific effect on Dcp2-mediated decay pathways. The K333A mutant of Dcp2 also led to stabilization of *RRP41* when this mutant was expressed on a *DCP2* KO background in HEK293T cells (Figure S6a-b), supporting functional importance of the Dcp2 C-terminus to which CP21 binds.

To more directly measure RNA decapping in cells, we performed a splinted ligation assay to quantify decapped RNA, which accumulates to detectable concentrations in yeast or mammalian cells lacking the downstream exonuclease Xrn1 (Blewett et al., 2011; Luo et al., 2020). We measured the decapping of the *HOXA13* RNA in *XRN1* KO cells (20) treated with 2  $\mu$ M CP21, D-CP21 or vehicle (Figure 4d). The transient accumulation of decapped *HOXA13* RNAs (the product of Dcp2 activity) was specifically abolished in CP21-treated cells. These results demonstrate that CP21 stabilizes RNAs by inhibiting either the decapping activity of Dcp2, or its interaction with RNA substrates, in cells.

CP21 inhibition of Dcp2 might be expected to phenocopy knockout, silencing or inactivating mutation of Dcp2. P-bodies are cytoplasmic liquid domains enriched in translationally repressed RNAs in complex with RNA decay-associated proteins (Eulalio et al., 2007; Luo et al., 2018). Deletion or silencing of Dcp2 has been shown to increase P-body numbers in yeast (Sheth and Parker, 2003) and mammalian cells (Aizer et al., 2014), possibly due to accumulation of deadenylated RNA decay intermediates in complex with proteins that can phase separate at high local concentrations. We observed that expression of the Dcp2 K333A mutant (in *DCP2* KO cells) caused a modest but statistically significant 1.3-fold increase in P-body numbers relative to expression of wild-type Dcp2, suggesting that this mutation is inactivating, consistent with the RNA decay measurements (Figure S6c). We then asked whether CP21 treatment would also affect P-body numbers. Indeed, CP21 increased P-body numbers compared to vehicle-treated cells (Figure 4e; average 1.4-fold increase), while P-body numbers in D-CP21 treated cells remained unaltered. Taken together, our RNA stability, decapping, and P-body imaging data suggest that CP21 inhibits decapping of specific endogenous reporter RNAs by Dcp2 in cells.

#### CP21 enables identification of new Dcp2 substrates

To explore the utility of CP21 in mapping of RNA substrates of Dcp2, we assessed the impact of CP21 on RNA stability using TimeLapse-seq in wild-type (WT) and *DCP2* KO HEK293T cells pre-treated with D-CP21 or CP21 (2  $\mu$ M, 5 h) using previously reported conditions (Luo et al., 2020). This shortened treatment time (5 h compared to 18 h for previous experiments) was chosen to minimize compensatory responses to Dcp2 inhibition and led to partial stabilization of an endogenous reporter RNA substrate relative to the 18 h treatment (*RRP41*, Figure 5a). We assigned 104 RNAs as specifically stabilized by CP21 using previously established criteria (Luo et al., 2020). Briefly, RNAs that are significantly upregulated at total RNA level in CP21 vs D-CP21 treated cells were assigned as dominantly decay-regulated if  $\log_2 \left| \frac{\Delta k_{deg}}{\Delta k_{syn}} \right| > 0$ , where  $k_{deg}$  and  $k_{syn}$  refer to the rate of RNA decay and synthesis, respectively. A majority (91 transcripts; Figure 5b, red) exhibited a smaller relative change of decay rate ( $\frac{\Delta k_{deg}}{\Delta k_{syn}}$ ) in *DCP2* KO vs WT HEK293T cells under the same set of treatment and were therefore defined as Dcp2 substrates (Figure 5b and Table S1). Most of these CP21-stabilized RNAs (84%) were not identified in our previous report on Dcp2 substrates (Luo et al., 2020). We hypothesized that these substrates were previously undetected as a result of secondary, compensatory effects of *DCP2* genetic ablation that obscured variation at total RNA level – a criterion used for Dcp2 substrate identification in our prior report. We selected several CP21-stabilized transcripts identified in our current study, and reanalyzed previously reported changes in their decay and synthesis rates in *DCP2* KO vs WT HEK293T cells (Luo et al., 2020). Indeed, 58% exhibited a decreased decay rate in the *DCP2* KO relative to WT, among which 68% evidenced a simultaneous decrease in RNA synthesis and therefore no significant change in total RNA level in *DCP2* KO cells (Figure 5c). This trend is evident in TimeLapse-seq sequencing tracks of these RNAs in *DCP2* KO vs WT cells (Figure 5d).

We validated several new Dcp2 substrates revealed by CP21 inhibition using cell-based RNA decay assays. First, we confirmed by qRT-PCR that RNA stabilization after transcriptional arrest is specific to CP21 treatment as compared to treatment with the D-CP21 control for six RNAs that were stabilized in the TimeLapse-seq dataset, either included in (*RFX7*, *ARHGAP32*, *PAX6*) or absent from (*SRSF12*, *ANKRD13A*, *ERGIC2*) our previous Dcp2 substrates list (Figure 6a and Figure 5d). To corroborate the observed stabilization as depending on Dcp2 inhibition, half-lives of the same RNAs in *DCP2* KO cells were then compared to those in WT HEK293T cells after transcriptional arrest (Figure 6b). RNA stability was greater in the *DCP2* KO cells relative to WT HEK293T for all tested transcripts, and the half-life of each transcript in *DCP2* KO cells was comparable to half-lives observed upon CP21 treatment, showing that CP21 has no effect on RNA stability in cells lacking Dcp2. Lastly, we performed qSL-RT-PCR for one of the newly identified Dcp2 substrates, *ERGIC2*, to confirm inhibition of Dcp2 decapping activity toward this transcript. CP21, but not D-CP21, abolished the accumulation of decapped *ERGIC2* intermediates in *XRN1* KO cells (Figure 6c), identical to genetic depletion of Dcp2 on the *XRN1* KO background (Figure 6d). Taken together, these data suggest that CP21-stabilized RNAs are cellular decapping substrates of Dcp2.

#### DISCUSSION

In this work, we developed a cell-permeable bicyclic peptide inhibitor of Dcp2 activity in human cells. Importantly, this inhibitor, CP21, binds to Dcp2 in cell lysates and cells, supported by photo-cross-linking and CETSA experiments. The specificity of CP21 for Dcp2 binding and inhibition is further supported by the inactivity of its enantiomer, D-CP21, which is otherwise identical in amino acid composition and charge, and its inability to alter reporter RNA half-lives relative to D-CP21 in *DCP2* KO cells. Further supporting inhibition of Dcp2 by CP21, a significant increase in cellular P-body numbers was observed upon CP21, but not D-CP21 treatment, phenocopying the effects of perturbed RNA decay described in prior reports (Sheth and Parker, 2003) and likely due to local accumulation of deadenylated RNA that cannot be decapped by Dcp2, leading to phase separation. CP21 may exert its cellular effect on Dcp2 activity by decreasing association of DDX6 with the decapping complex, supported by decreased co-immunoprecipitation of DDX6 with CP21-treated decapping complexes as well as destabilization of DDX6 by CP21. DDX6 plays a role in recognizing inefficiently translated RNAs and promoting their decay (Mugridge et al., 2018a). We therefore speculate that CP21 prevents delivery of RNA substrates to the decapping complex by DDX6. However, because DDX6 does not directly bind to Dcp2, the mechanism by which DDX6 occupancy is perturbed by CP21 is likely indirect and requires further elucidation.

In addition to directly binding the Nudix domain of Dcp2, we found evidence that CP21 interacts with a C-terminal disordered region of Dcp2, and in particular that CP21 requires the K333 residue for Dcp2 binding. We demonstrate the

importance of this region in human Dcp2 by showing that Dcp2 target decay rates are slowed and P-bodies are increased by the K333A Dcp2 mutation. These results are consistent with a requirement for K333 for Dcp2 function, which can be blocked either via mutation to alanine or binding to CP21. This residue, which lies within an intrinsically disordered region unique to human Dcp2, has not been previously biochemically characterized, and the mechanism by which it contributes to Dcp2 regulation remains unclear.

Global profiling of RNA levels using TimeLapse-seq in WT and *DCP2* KO HEK293T cells pre-treated with CP21 revealed Dcp2-dependent stabilization of 91 RNAs that were not stabilized in the D-CP21 control. 15 of these RNAs, mostly transcription factors, were previously identified as Dcp2 substrates (Luo et al., 2020). Inspection of the 76 novel Dcp2 substrates identified here reveal splicing and transcription factors, as well as proteins involved in signal transduction (e.g. GTPases), among other important functions. Importantly, 52% of CP21-stabilized RNAs identified in this work were upregulated by DDX6 silencing in a previous study (Courel et al., 2019), consistent with decreased DDX6 association with the decapping complex after CP21 treatment. We provided evidence that many Dcp2 substrates identified in this study were previously masked by increased synthesis rates in *DCP2* KO cells, demonstrating the value of acute inhibition in overcoming genetic compensation.

While this study successfully identified a number of novel Dcp2 targets, several important questions remain. First, only 91 transcripts were stabilized by CP21 — far fewer than the 1800 Dcp2 substrates previously identified using genetic knockout (Luo et al., 2020). This may be due to incomplete inhibition of Dcp2 by CP21 in the substrate discovery experiment, first and foremost because of the short pretreatment used in the TimeLapse-seq experiments (Figure 5a). It is also likely that CP21 is not fully membrane permeable, leading to low effective concentration of the inhibitor within the cytosol. *In vitro* IC<sub>50</sub> measurements would be necessary to determine if Dcp2 is fully inhibited at the experimental CP21 concentration and treatment times. Another possible explanation could be context dependence of the experiments; for example, if cell penetration by CP21 activates cellular stress responses (Ng et al., 2020), differential gene expression could lead to detection of Dcp2 substrates upregulated under these conditions relative to *DCP2* KO cells in which stress responses have not been activated. It is alternatively possible that CP21 inhibits decay of a specific subset of Dcp2 targets. Supporting this hypothesis, the Dcp2 substrates identified in this study, as a class, diverge in their properties from Dcp2 substrates identified in *DCP2* KO cells. For example, 60% of Dcp2 targets identified in this work are depleted from P-bodies relative to the cytoplasm — close to the proportion of RNAs in the whole transcriptome that are depleted from P-bodies (Hubstenberger et al., 2017) — in contrast to our previous study of Dcp2 substrates, a majority of which were enriched in P-bodies (Luo et al., 2020). This suggests that CP21 may inhibit activity toward a subset of Dcp2 substrates partly distinct from those stabilized by genetic knockout. Taken together with the observation that CP21 treatment decreases DDX6 association with the decapping complex, we suggest that the Dcp2 substrates identified in the TimeLapse-seq experiment are most likely the subset of RNAs most dependent on DDX6 for Dcp2 targeting. It is possible that binding of CP21 to Dcp2 specifically disrupted presentation of these DDX6-associated RNAs to the decapping complex (Figure 7). In a study of yeast Dcp2 active site vs C-terminal mutants, differential stabilization of RNA substrates by different mutations was observed, providing precedent for this hypothesis (He et al., 2018).

In summary, this study reports a Dcp2 ligand that can be used to inhibit the decay of specific Dcp2 substrates and increase membraneless organelle formation. Application of CP21 in global profiling of Dcp2 substrates reiterates the complexity of human 5'-3' RNA decay and extends our knowledge of Dcp2 substrate specificity. Future efforts that focus on further biochemical and structural characterization of the Dcp2-CP21 interaction; determination of the effect of CP21 on Dcp2 structure, interactions, and activity in cells; and systematic evaluation of the cellular uptake of CP21 may provide new insights into the molecular and conformational control of Dcp2 activity.

## SIGNIFICANCE

RNA decapping, or the removal of the 7-methylguanosine (m<sup>7</sup>G) cap, gates entry into 5'-to-3' RNA decay and regulates important processes including innate immune responses. In mammals, three Nudix family proteins decap RNA, with their functional specialization partially defined by prior studies based on traditional genetics. However, genetic compensation in decapping enzyme knockout cells has been observed, complicating substrate identification for these enzymes. Screening for small molecule inhibitors specific to each enzyme is challenging because of their similar, conformationally flexible active sites. Here, we demonstrate the selection and application of a stapled peptide inhibitor in discovery of human Dcp2 substrates. This study demonstrates how the development of inhibitors can disentangle the complex network of mammalian RNA decay factors.

## ACKNOWLEDGMENT

We thank Dr. Christian Heinis (Institute of Chemical Sciences and Engineering, Ecole Polytechnique Fédérale de Lausanne, Lausanne, CH) for providing phage vectors (fdg3p0ss21 and fd0D12) and expert advice. We thank Salman Saeed for his early works on cell permeability and the effect of CP21 on RNA stability and all members of the Slavoff lab for helpful discussion and comments on the manuscript. We also thank Prof. J. Ellman, A. Saghatelian, and J. Crawford for valuable suggestions on the project. This work was supported in part by the NIH (R01GM122984), the Searle Scholars Program, a Catalyst Award from the Dr. Ralph and Marian Falk Medical Research Trust, and Yale University West Campus start-up funds (to S.A.S.) and by NIH Grant DP2 HD083992-01 (to M.D.S.). J. A. S. was in part supported by an NIH Predoctoral Training Grant (T32GM007223).

### AUTHOR CONTRIBUTIONS

Y.L. designed and performed experiments and data analysis and wrote the manuscript. J.A.S and M.D.S. designed and performed TimeLapse-seq experiments and data analysis and edited the manuscript. Z.N. generated KO cells and performed mass spectrometry experiments. T.H. performed the CETSA. S.A.S conceived the project, designed experiments and edited the manuscript. All authors have given approval to the final version of the manuscript.

### DECLARATION OF INTERESTS

The authors declare no conflict of interests.

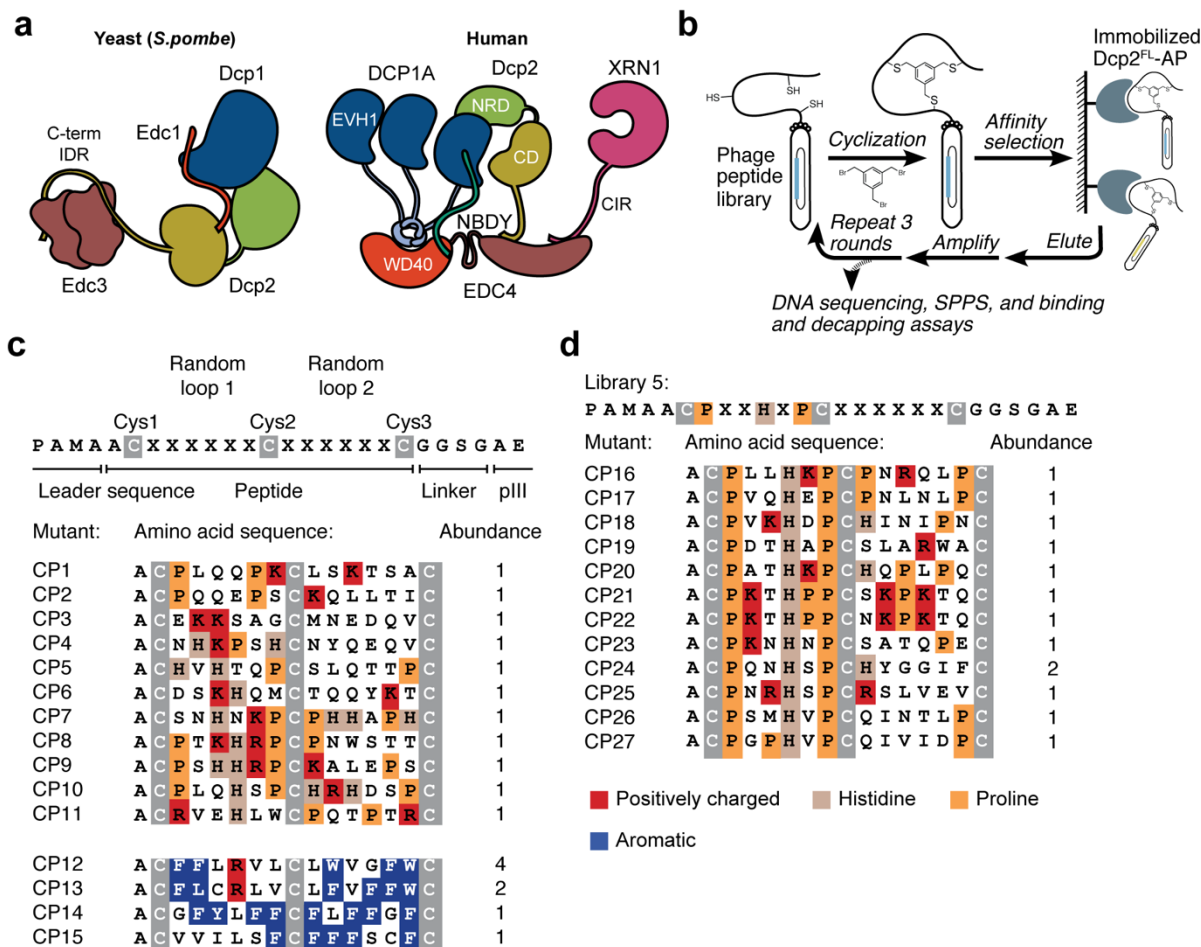


**Figure 1. Phage display selection of bicyclic peptides to identify ligands of human Dcp2 (Dcp2).** (a) Cartoon representation of the yeast and human Dcp2 decapping complexes (adapted and updated from Chang et al., 2014 and Paquette et al., 2018). IDR, intrinsically disordered region; NRD, N-terminal  $\alpha$ -helical regulatory domain; CD, Nudix catalytic domain; CIR, C-terminal interacting region. (b) Schematic illustration of the strategy to select Dcp2 binders from a phage-displayed 6x6 peptide library containing 3 fixed cysteine residues for chemical cyclization with 1,3,5-tris(bromomethyl)benzene (TBMB). SPPS, solid phase peptide synthesis. (c) Sequences of two classes of selected bicyclic peptides enriched by a site-specifically biotinylated Dcp2 construct, Dcp2<sup>FL</sup>-AP (see Figure S1). Positively charged residues are highlighted in red, histidine taupe, prolines orange, and aromatic residues blue. (d) Amino acid sequences of selected clones from affinity maturation with Dcp2<sup>FL</sup>-AP. All clones derive from library 5, designed around proline-rich sequences enriched from the initial fully random library (b, top).



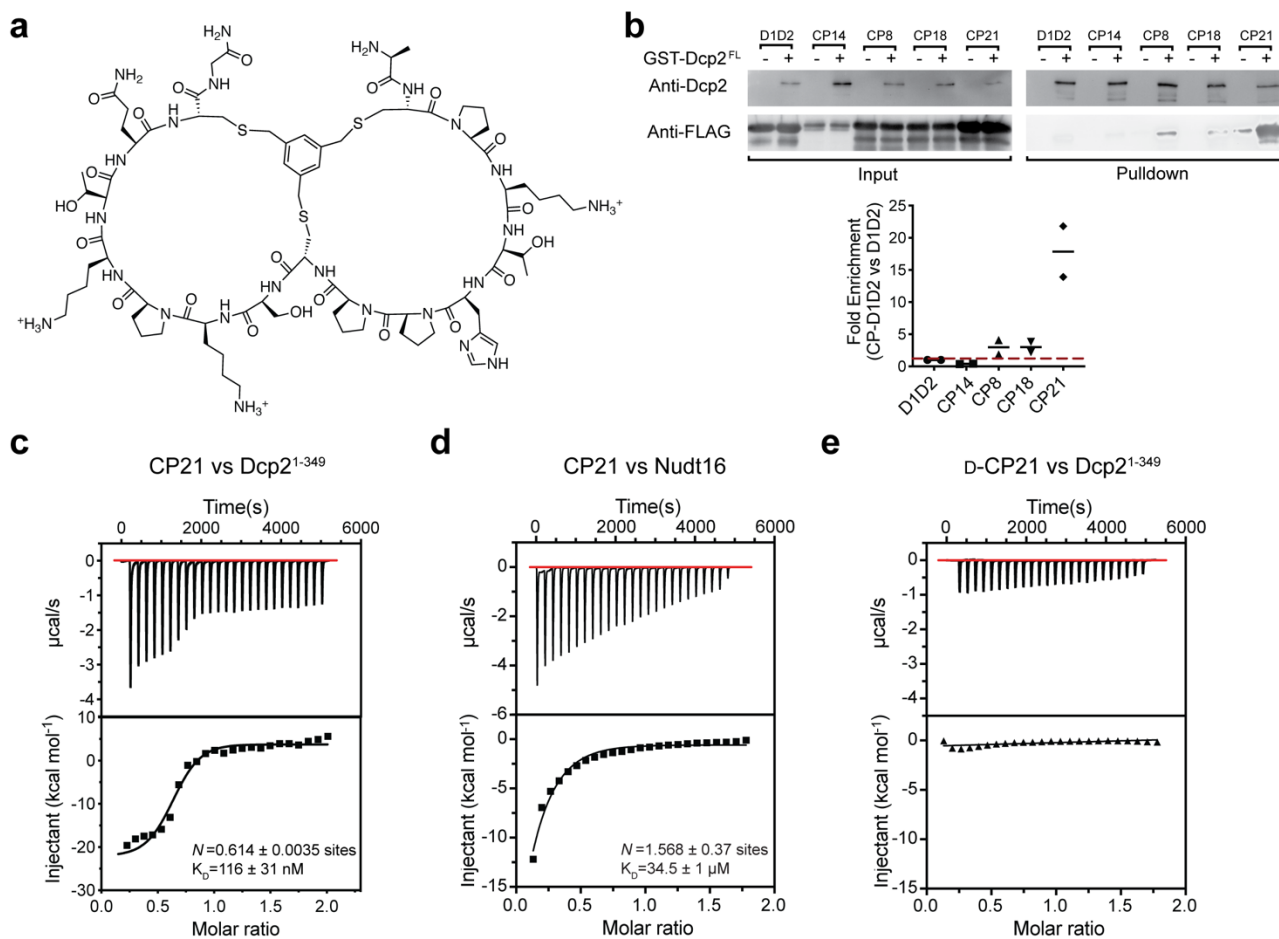


**Figure 2. Cyclic peptide CP21 binds to Dcp2 *in vitro*.** (a) Structure of synthesized CP21. (b) Validation of Dcp2 binding to selected TBMB-cyclized peptides by *in vitro* pull-down assay. Phage-display-enriched CP sequences were cloned as fusions to the cysteine-free D1D2 domain of phage pIII protein for bacterial expression, biochemically purified and cyclized with TBMB. GST-Dcp2<sup>FL</sup> was co-incubated with 10-fold molar excess of the FLAG epitope-tagged CP-D1D2 fusion proteins, with D1D2 alone as a negative control, and GST pull-down was performed prior to western blot detection. Representative data of two technical replicates are shown. Lines from the scatter plot indicate the mean value of CP-D1D2 enrichment. (c-e) Isothermal calorimetry (ITC) titrations of chemically synthesized CP21 to Dcp2<sup>1-349</sup> (c), CP21 to Nudt16 (d), and D-CP21 to Dcp2<sup>1-349</sup> (e), respectively. Data shown are representative of two technical replicates, and dissociation constant is reported as  $\pm$  the error of fitting.

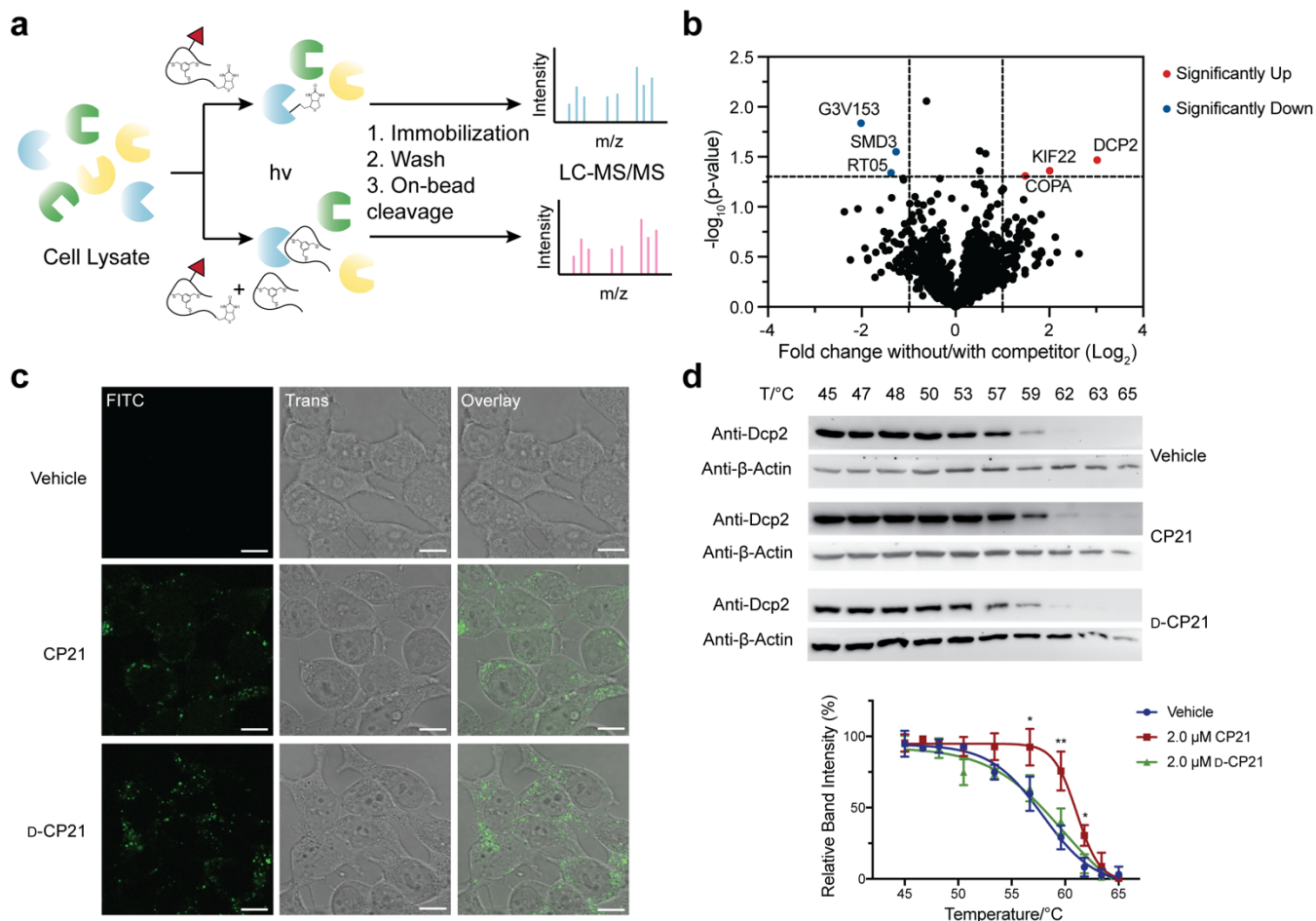


**Figure 3. CP21 binds to Dcp2 in cells.** (a) Schematic representation of the target ID workflow. Cell lysates are incubated with biotinylated Photo-CP-3 in the absence (top) or presence (bottom) of excess CP21 as a competitor. After irradiation (hv), cross-linked and biotinylated proteins are immobilized, washed, trypsinized and subjected to LC-MS/MS proteomics with label-free quantitation. Red triangle, photo-cross-linker. (b) Volcano plot of protein enrichment ratios (without/with 5-fold excess unlabeled CP21 as competitor) and p-values from target ID experiments ( $n=3$ ). (c) Assessment of cellular uptake of the cyclic peptides by live-cell confocal fluorescence microscopy of HEK293T cells incubated with vehicle or FITC-labeled CP21 in either all-L or all-D form (3  $\mu$ M, 5 h). Z-plane scanning was performed to minimize signal from cell surface. Images are representative of two independent experiments. Scale bars, 10  $\mu$ m. Trans, transillumination. (d) Cellular thermal shift assay (CETSA) of Dcp2 in the presence and absence of 2  $\mu$ M CP21 in intact HEK293T cells. D-CP21 was used as a negative control. Significant differences in Dcp2 intensity (band densitometry) at 57, 59 and 62  $^{\circ}$ C were analyzed by one-way ANOVA. Number of biological repeats:  $n=3$ . Error bars represent  $\pm$  s.d. P-values (with Dunnett's test) are denoted by asterisks; (\*)  $p<0.05$ ; (\*\*)  $p<0.01$ .

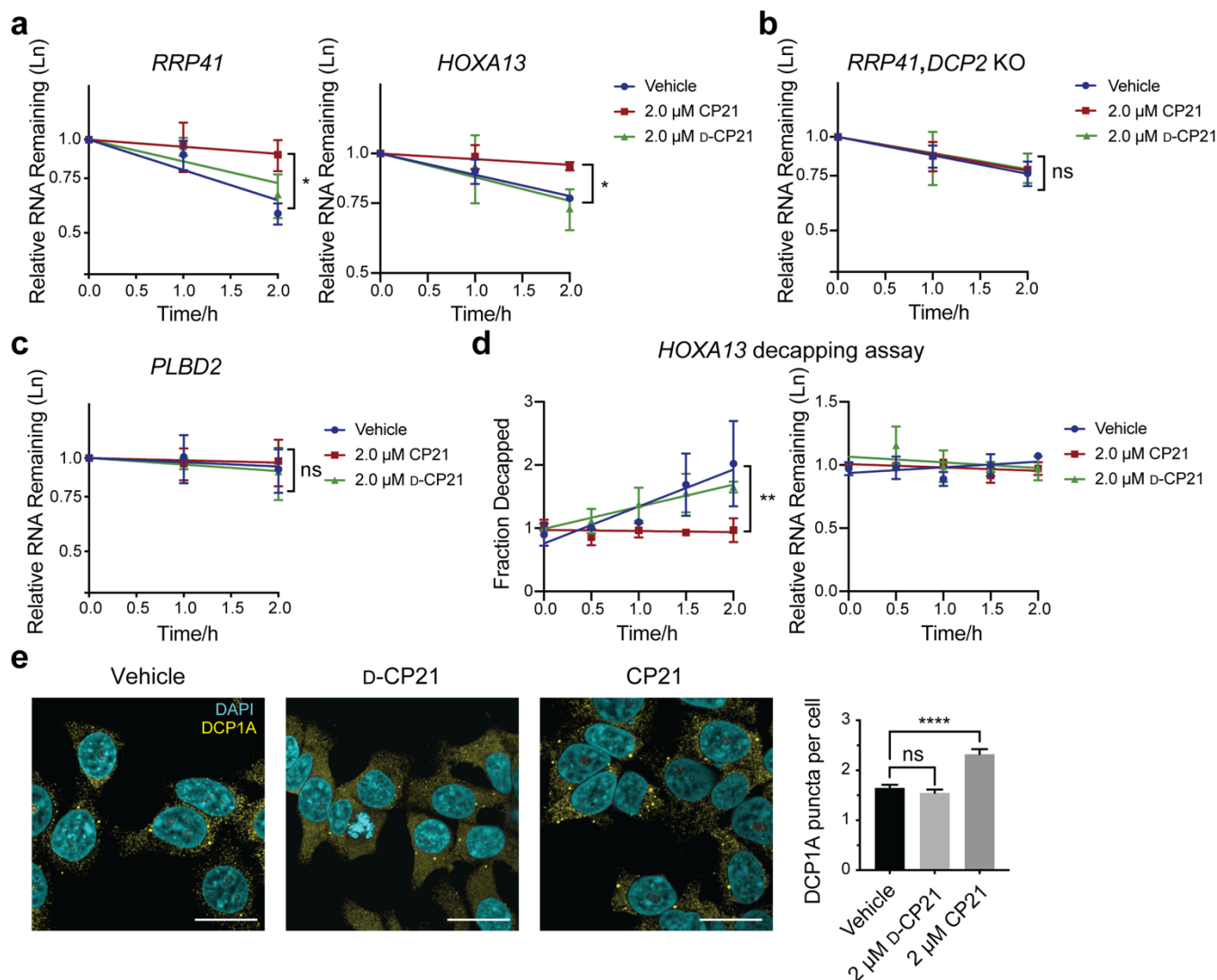


**Figure 4. CP21 stabilizes specific cellular Dcp2 targets at the decapping step.** (a) RNA decay curves of selected Dcp2 targets from HEK293T cells treated with 2  $\mu$ M of CP21 (red), D-CP21 (green), or vehicle (equal volume of peptide storage buffer, blue). Relative levels of each RNA remaining at indicated time points following actinomycin D treatment were determined by quantitative reverse transcription PCR (qRT-PCR, see methods). Error bars represent mean  $\pm$  s.d. Number of biological repeats:  $n=3$ . Significance was derived from one-way ANOVA of the slope of regression lines; (\*)  $p<0.05$ . (b) Decay of *RRP41* RNA in *DCP2* KO HEK293T cells treated with CP21, D-CP21, or vehicle. Number of biological repeats:  $n=3$ . Error bars represent  $\pm$  s.d. P-values (ANOVA linear regression with Dunnett's test) are denoted by asterisks; (ns) non-significant. (c) *PLBD2*, the stability of which is not affected by Dcp2, was not stabilized by CP21 according to qRT-PCR analysis. Number of biological repeats:  $n=3$ . Error bars represent  $\pm$  s.d. and significance was evaluated with ANOVA linear regression; (ns) non-significant. (d) Splinted ligation RT-PCR (qSL-RT-PCR) assay was used to detect decapped RNA under CP21 treatment. The relative fraction decapped *HOXA13* transcripts following transcriptional block for the indicated times in *XRNI* KO cells treated with CP21, D-CP21, or vehicle was normalized to  $t = 0$  (left). The mean of three biological replicates was plotted. Error bars represent  $\pm$  s.d. Significance at all time points was analyzed by ANOVA linear regression (with Dunnett's test); (\*\*)  $p<0.01$ . Total RNA level of *HOXA13* in *XRNI* KO cells from the same samples measured by qRT-PCR suggested treatment with neither compound affects total RNA level in *XRNI* KO (right). (e) P-body numbers in HEK293T cells treated with 2  $\mu$ M CP21, D-CP21, or the same volume of vehicle for 18 h. Fixed cells were stained with antibodies detecting DCP1A, a P-body marker. Six fields of view ( $\geq 180$  cells) were used to quantitate average P-bodies per cell in each condition. P-body numbers were counted using ImageJ as previously described (see Methods). Data represent mean values  $\pm$  s.e.m, and significance was evaluated with one-way ANOVA (with Dunnett's test); (ns) non-significant, (\*\*\*\*)  $p<0.0001$ . Scale bars, 25  $\mu$ m.

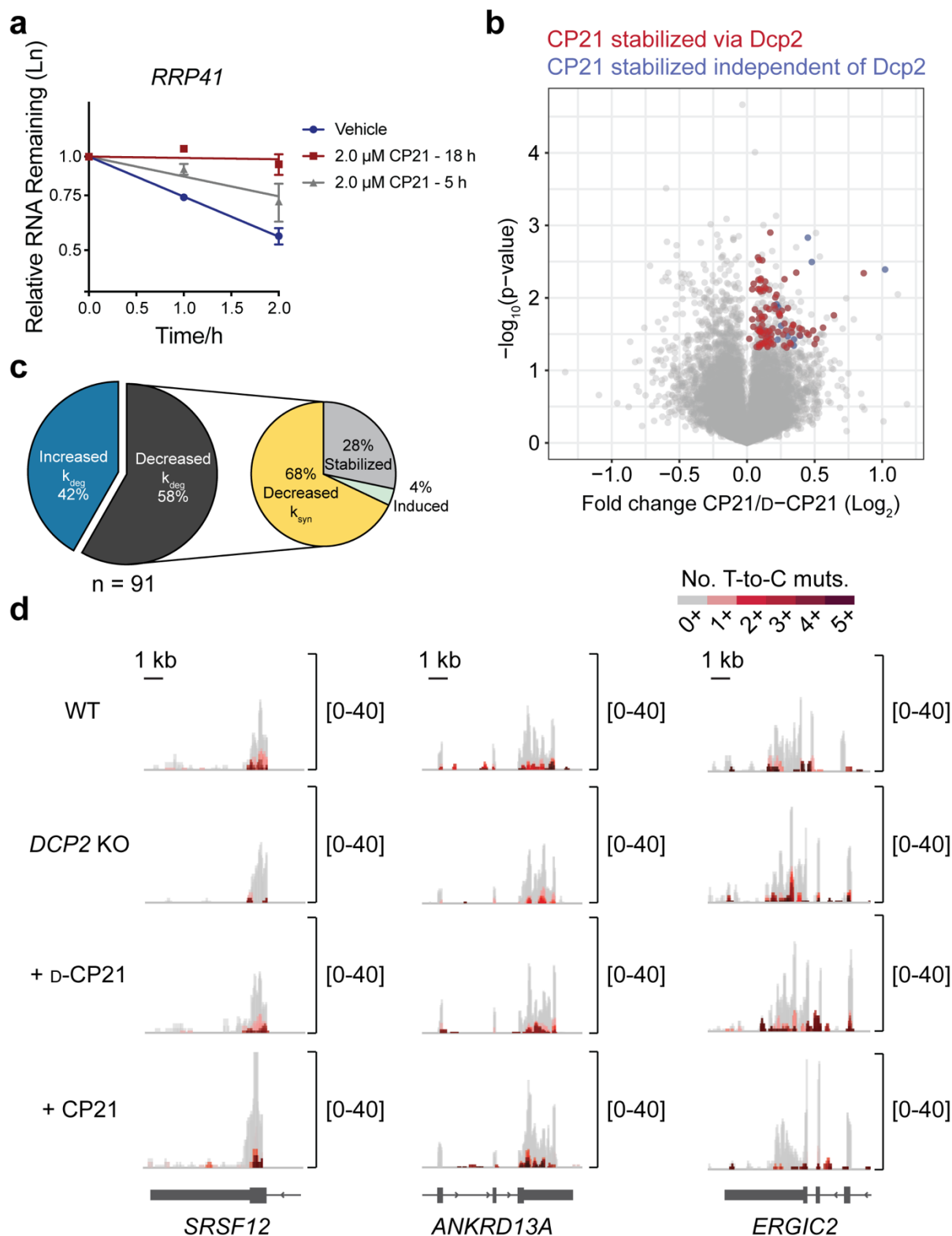


**Figure 5. TimeLapse-seq profiling of CP21-stabilized RNAs enables identification of new cellular Dcp2 targets.** (a) Validation of CP21 treatment scheme for TimeLapse-seq experiments. *RRP41* RNA decay curves of HEK293T cells treated with 2  $\mu$ M CP21 for 5 h vs 18 h. The levels of *RRP41* RNA remaining following actinomycin D treatment at indicated time points relative to  $t = 0$  h were determined by qRT-PCR, with Ct value normalized to U6 based on previous reports (Li et al., 2008). Number of biological repeats:  $n=2$ . (b) Volcano plot of TimeLapse-seq analysis (2 h sU labeling period) from HEK293T cells pre-treated with 2  $\mu$ M CP21 vs D-CP21 for 5 h.  $\text{Log}_2(\text{Fold Change})$  in total RNA is calculated from CP21/D-CP21, and Dcp2-dependent stability changes (red) were identified by comparing relative change in decay vs synthesis rate for CP21-stabilized RNAs (red and blue) in WT to *DCP2* KO cells under the same CP21 vs D-CP21 treatment scheme (see Methods). Data represent two biological replicates. (c) Analysis of RNA decay rate ( $k_{\text{deg}}$ ) or synthesis rate ( $k_{\text{syn}}$ ) changes in *DCP2* KO vs WT HEK293T cells of Dcp2-dependent, CP21-stabilized RNAs. (d) TimeLapse-seq tracks of three newly identified Dcp2 targets in HEK293T cells pretreated with CP21 vs D-CP21 (2  $\mu$ M, 5 h) were compared to that in untreated WT vs *DCP2* KO HEK293T cells. Increasing T-to-C mutational content indicates higher recoded sU incorporation over the 2 h metabolic labeling period for newly synthesized mature RNA.

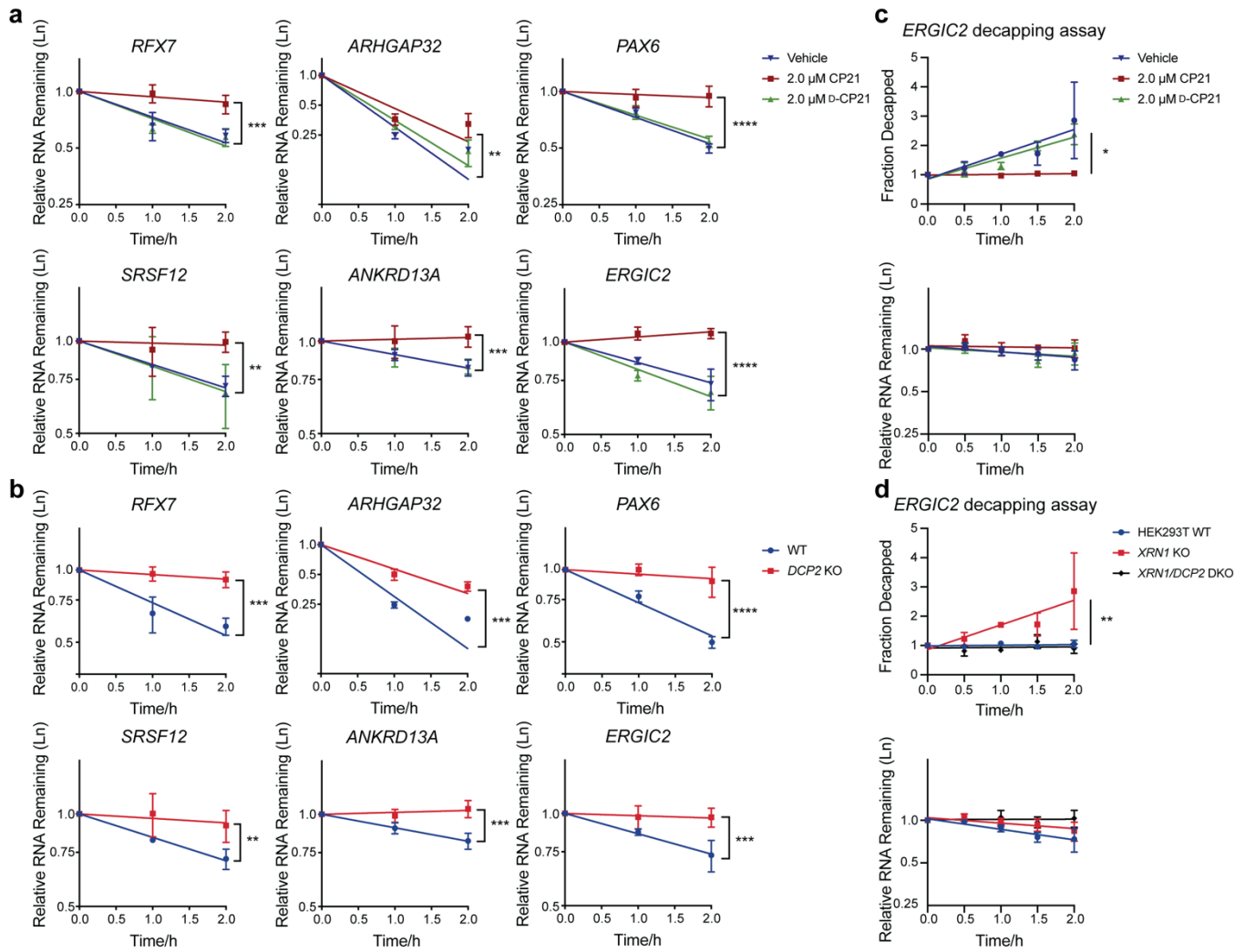


**Figure 6. CP21-stabilized transcripts are cellular Dcp2 substrates.** (a) The RNA lifetime of selected transcripts stabilized by CP21 were measured using transcriptional arrest and qRT-PCR. HEK293T cells were treated with 2  $\mu$ M of CP21 (red), D-CP21 (green), or vehicle (blue), then subjected to actinomycin D-mediated transcriptional arrest for the indicated times. Relative RNA levels were normalized to  $\beta$ -actin. Number of biological replicates:  $n=4$ . Error bars represent  $\pm$  s.d. Significance was derived from one-way ANOVA of the slope of regression lines; (\*\*)  $p<0.01$ ; (\*\*\*)  $p<0.001$ ; (\*\*\*\*)  $p<0.0001$ . (b) The stabilities of the same set of CP21 RNA targets were measured in DCP2 KO (red) vs WT (blue) HEK293T cells treated with actinomycin D for the indicated times. Number of biological replicates:  $n=4$ . Significance was calculated from linear regression  $t$ -test. (c) The fraction decapped ERGIC2 transcripts detected by qSL-RT-PCR in XRN1 KO cells treated with 2  $\mu$ M CP21 (red), D-CP21 (green), or the same volume of vehicle (blue) at the indicated time points following actinomycin D treatment (top). Total RNA levels from the same samples were measured by qRT-PCR (bottom). (d) qSL-RT-PCR performed in wild-type (WT), XRN1 KO and XRN1/DCP2 double knockout (DKO) HEK293T cell lines to analyze decapping of ERGIC2 transcript (top). Total RNA levels were derived from qRT-PCR of the same samples (bottom). Number of biological replicates:  $n=3$ . Error bars represent the mean  $\pm$  s.d. Significance was analyzed by ANOVA linear regression (Dunnett's test); (\*)  $p<0.05$ ; (\*\*)  $p<0.01$ .

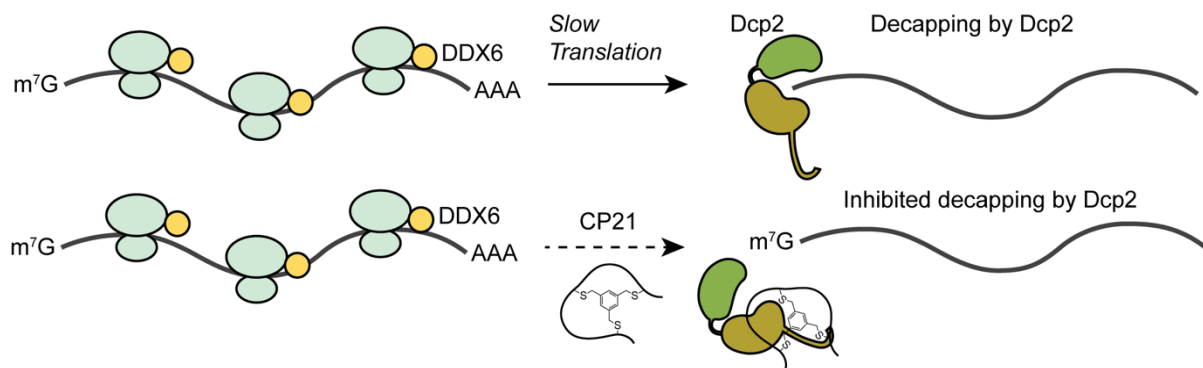


**Figure 7. CP21 inhibits decapping of subgroups of RNAs by human Dcp2 in cells: a model.** DDX6 associates with slowly translated mRNAs and couples translation efficiency with 5'-to-3' RNA decay (Mugridge et al., 2018a). CP21 weakens the interaction between DDX6 and the Dcp2-containing decapping complex, thus inhibit decapping of specific RNAs.

## STAR METHODS

### KEY RESOURCES TABLE

REAGENT or RESOURCE	SOURCE	IDENTIFIER
Antibodies		
Mouse monoclonal anti-FLAG	Sigma-Aldrich	Cat#F3165; RRID:AB_259529
Rabbit polyclonal anti-Dcp2	Novus Biologicals	Cat#NBP1-41070; RRID:AB_2230386
Mouse monoclonal anti- $\beta$ -actin	Invitrogen	Cat#BA3R; RRID:AB_10750953
Rabbit polyclonal anti-DCP1A	Sigma-Aldrich	Cat#D5444; RRID:AB_1840794
Rabbit polyclonal anti-GST tag	GenScript	Cat#A00202; RRID:AB_914657
Rabbit polyclonal anti-DDX6	abcam	Cat#ab103308; RRID:AB_10711805
Rabbit polyclonal anti-EDC3	abcam	Cat#ab168851; RRID:AB_2715533
Rabbit polyclonal anti-COPA	Bethyl	Cat#A304-515A; RRID:AB_2620709
Goat anti-rabbit peroxidase conjugate	Rockland	Cat#611-103-122; RRID:AB_218567
Goat anti-mouse peroxidase conjugate	Rockland	Cat#610-1319; RRID:AB_219659
Goat anti-rabbit Alexa Fluor 568	Life Technologies	Cat#A-11011; RRID:AB_143157
Bacterial and Virus Strains		
<i>E.coli</i> TG1	Lucigen	Cat#60502
<i>E.coli</i> BL21 Gold (DE3)	Invitrogen	Cat#C600003
<i>E.coli</i> Rosetta (DE3)	Novagen	Cat#70954
fd0D12	Heinis et al., 2009	N/A
fdg3p0ss21	Kather et al., 2005	N/A
Chemicals, Peptides, and Recombinant Proteins		
FBS	Sigma-Aldrich	Cat#F4135
Penicillin-Streptomycin (10,000 U/mL)	VWR	Cat#97063-708
Tris(2-carboxyethyl)phosphine (TCEP)	Sigma-Aldrich	Cat#C4706; CAS: 51805-45-9
Ethylenediaminetetraacetic acid (EDTA)	MP Biomedicals	Cat#152521; CAS:6381-92-6
1,3,5-tris(bromomethyl)benzene	Santa Cruz Biotechnology	Cat#sc-476521; CAS:18226-42-1
Isopropyl $\beta$ -D-thiogalactoside (IPTG)	AmericanBIO	Cat#AB00841; CAS:367-93-1
Polyethylene glycol (PEG-6000)	Santa Cruz Biotechnology	Cat#sc-302016A; CAS:25322-68-3
Lysozyme	DOT Scientific	Cat#DSL38100-10
DNase I	NEB	Cat#M0303
Streptavidin-HRP	Thermo Fisher	Cat#S911
cOmplete Mini, EDTA-free protease inhibitor cocktail	Roche	Cat#11836170001
TRIzol reagent	Thermo Fisher	Cat#15596018
Fibronectin, human	Sigma-Aldrich	Cat#FC010
Formalin, buffered, 10%	Fisher Chemical	Cat#SF100; CAS: 50-00-0
4-thiouridine	Thermo Fisher	Cat#AAJ60679-MD; CAS: 13957-31-8



2,2,2-trifluoroethylamine	Thermo Fisher	Cat#AC303500010; CAS:753-90-2
Sodium periodate	Thermo Fisher	Cat#AC419610050; CAS:7790-28-5
DTT	DOT Scientific	Cat#DSD11000-5
Ammonium bicarbonate	J.T.Baker	Cat#3003-01; CAS:1066-33-7
Critical Commercial Assays		
Free thiol assay kit (fluorometric)	abcam	Cat#ab112158
iScript cDNA synthesis kit	Bio-Rad	Cat#1708891
SMARTer Stranded Total RNA-Seq Kit v2 - Pico Input Mammalian	Takara Bio	Cat#634413
Deposited Data		
TimeLapse-seq data	This paper	GSE153258
Experimental Models: Cell Lines		
Human: HEK293T	ATCC	CRL-3216
Human: <i>DCP2</i> knock out HEK293T	Luo et al., 2020	N/A
Human: <i>XRNI</i> knock out HEK293T	Luo et al., 2020	N/A
Human: <i>DCP2/XRNI</i> dual knock out HEK293T	Luo et al., 2020	N/A
Oligonucleotides		
Primer: Dcp2-Fwd: AAAAGTCGACATGGAGACCAAACGGG	This paper	N/A
Primer: Dcp2-linker-Rev: TTTTCCAGAACCCGCCGACGACCTTCGATCGCCGCAAGGT CCAAGATTTTCATTATAGCATTATGGTCA	This paper	N/A
Primer: Dcp2-AP-Rev: TTTTCTCGAGACCAGAACCTTCGTGCCATTTCGATTTTCTGC GCTTCGAAGATGTCGTTTCAGACCAGAACCCGCCGACG	This paper	N/A
Primers for qRT-PCR, see Method Details	This paper	N/A
Recombinant DNA		
pET21a-BirA	Howarth et al., 2005	Addgene Cat#20857
pGEX-6P-3-Dcp2 <sup>n</sup>	This paper	N/A
pET21a-Dcp2 <sup>n</sup> -AP	This paper	N/A
pET28a-Dcp2 <sup>257</sup>	This paper	N/A
pET28a-Dcp2 <sup>260</sup>	This paper	N/A
pET21a-Dcp2 <sup>n</sup>	This paper	N/A
pcDNA3-FLAG-Dcp2 <sup>n</sup>	This paper	N/A
pET28a-CP21-D1D2-FLAG	This paper	N/A
pLJM1-EGFP	Sancak et al., 2008	Addgene Cat#19319
psPAX2	Trono Lab Packaging Plasmid (unpublished)	Addgene Cat#12260
pMD2.G	Trono Lab Envelop Plasmid (unpublished)	Addgene Cat#12259
Software and Algorithms		
Fiji	Schindelin et al., 2012	<a href="https://fiji.sc">https://fiji.sc</a>
MaxQuant	Cox and Mann, 2008	<a href="https://maxquant.net">https://maxquant.net</a>
Mascot	Perkins et al., 1999	<a href="http://www.matrixscience">http://www.matrixscience</a>
Perseus	Tyanova et al., 2016	<a href="https://maxquant.net/pers">https://maxquant.net/pers</a>
R (3.6.1)		<a href="https://cran.r-project.org/mirrors.html">https://cran.r-project.org/mirrors.html</a>
Python (2.7.11)		<a href="https://www.python.org/downloads/">https://www.python.org/downloads/</a>
Cutadapt (1.9.1)		<a href="https://github.com/marcelm/cutadapt">https://github.com/marcelm/cutadapt</a>



HTSeq (0.6.1)		<a href="https://github.com/simon-anders/htseq">https://github.com/simon-anders/htseq</a>
SAMtools (1.9)		<a href="https://github.com/samtools/samtools">https://github.com/samtools/samtools</a>
HISAT2 (2.1.0)		<a href="https://github.com/infphilo/hisat2">https://github.com/infphilo/hisat2</a>
BCFtools (1.5)		<a href="https://github.com/samtools/bcftools">https://github.com/samtools/bcftools</a>
Picard (2.21.1)		<a href="https://github.com/broadinstitute/picard">https://github.com/broadinstitute/picard</a>
STAR (2.7.1)		<a href="https://github.com/alexdobin/STAR">https://github.com/alexdobin/STAR</a>
Tidyverse (1.2.1)		<a href="https://github.com/tidyverse/tidyverse">https://github.com/tidyverse/tidyverse</a>
edgeR (3.28.0)		<a href="http://bioinf.wehi.edu.au/edgeR">http://bioinf.wehi.edu.au/edgeR</a>
MASS (7.3-51.4)		<a href="http://www.stats.ox.ac.uk/pub/MASS4/">http://www.stats.ox.ac.uk/pub/MASS4/</a>
Rsamtools (2.2.1)		<a href="http://bioconductor.org/packages/Rsamtools">http://bioconductor.org/packages/Rsamtools</a>
Multidplyr (0.0.0.9000)		<a href="https://github.com/hadley/multidplyr">https://github.com/hadley/multidplyr</a>
Optparse (1.6.4)		<a href="https://github.com/trevorltd/r-optparse">https://github.com/trevorltd/r-optparse</a>

## METHOD DETAILS

**Lead Contact.** Further information and requests for resources and reagents should be directed to and will be fulfilled by the Lead Contact, Sarah Slavoff (sarah.slavoff@yale.edu)

**Materials Availability.** Reagents generated in this study are available on request with a completed Materials Transfer Agreement.

**Data and code availability.** All TimeLapse-seq data were submitted to GEO (accession code GSE153258; full data can be accessed using this link with the following reviewer's token crolkeyepxuhdwf: <https://www.ncbi.nlm.nih.gov/geo/query/acc.cgi?acc=GSE153258>). All software and parameters used are described below, and custom scripts and functions will be made available upon request.

**Cell Culture.** HEK293T cells were purchased from ATCC, and early-passage stocks were maintained to ensure cell line provenance and sterility. *DCP2* KO and *XRN1* KO HEK293T cells were generated using gRNAs to target the genomic region, as described earlier (Luo et al., 2020). All cells were maintained in DMEM (Invitrogen) supplemented with 10% (vol/vol) FBS and 100 U/mL penicillin-streptomycin. Cells were verified to be mycoplasma-free using the ATCC Universal mycoplasma detection kit.

**Antibodies.** Primary antibodies used for western blotting and/or immunofluorescence were as follows: mouse monoclonal anti-FLAG (Sigma, F3165); rabbit polyclonal anti-Dcp2 (Novus Biologicals, NBP1-41070); mouse monoclonal anti-beta actin (Invitrogen, BA3R); rabbit polyclonal anti-DCP1A (Sigma, D5444); rabbit polyclonal anti-GST-tag (GenScript, A00202); rabbit polyclonal anti-DDX6 (abcam, ab103308); rabbit polyclonal anti-EDC3 (abcam, ab168851); rabbit polyclonal anti-COPA (Bethyl, A304-515A), and streptavidin horseradish peroxidase conjugate (Thermo Fisher, S911). Secondary antibodies for western blotting were goat anti-rabbit peroxidase conjugate (Rockland, 611-103-122; Merck, AP132P) and goat anti-mouse peroxidase conjugate (Rockland, 610-1319). The secondary antibody for immunofluorescence was goat anti-rabbit Alexa Fluor 568 (Life Technologies, A-11011).

**Generation of phage peptide libraries.** The phage-encoded 6 x 6 peptide library was cloned into the fd0D12 vector (kindly provided by Dr. Christian Heinis and Dr. Simon Middendorp from the Institute of Chemical Sciences and Engineering in EPFL, Lausanne) with SfiI restriction sites. The cysteine-free D1D2 domain of phage pIII was amplified from fdg3p0ss21, and genes encoding the semi-random peptide sequence were appended to its N-terminus in two consecutive PCR reactions, as previously described by Heinis and co-workers (Rentero Rebollo and Heinis, 2013). The desalted ligation product was transformed into electrocompetent TG1 cells (Lucigen) and plated on 2-YT/chloramphenicol (30 µg/mL) agar plates. Colonies were scraped off from the plates with 2-YT media, supplemented with 15% glycerol and stored at -80 °C. The phage library was purified from 1-liter TG1 culture inoculated with the glycerol stock by polyethylene glycol (PEG) precipitation, and the infective virions were determined by plating 10-fold dilutions on 2-YT/chloramphenicol plates. The isolated phage was incubated with 1 mM tris(2-carboxyethyl) phosphine (TCEP) in 20 mL of degassed reaction buffer (5 mM EDTA, 20 mM NH<sub>4</sub>HCO<sub>3</sub>, pH 8.0) for 1 h at 42 °C to reduce all cysteines, followed by cyclization with 12.5 µM tris(bromomethyl)benzene (TBMB) in reaction buffer/acetonitrile (vol/vol=4:1) at 42 °C for 1 h and a final PEG precipitation step. A free thiol assay (Abcam) was utilized to confirm successful cyclization. Phage titer at all stages of phage production and cyclization was analyzed to ascertain that no significant loss of infective virions was observed.

**Cloning and genetic constructs.** His<sub>6</sub>-BirA was obtained from Addgene as a gift from A. Ting (Howarth et al., 2005) (Stanford University, Department of Genetics & Biology, Stanford, CA). For bacterial expression, full-length Dcp2 (Dcp2<sup>FL</sup>) was cloned into BamHI and SalI

sites of the pGEX-6P-3 vector (GE Life Sciences) together with a C-terminal His<sub>6</sub> tag or into Sall and XhoI sites of the pET21a(+) vector with a C-terminal AviTag peptide (AP)(Fairhead and Howarth, 2015) (Figure S1b). All truncations of Dcp2 were cloned into BamHI and XhoI sites of pET28a for affinity purification by His<sub>6</sub> tag (Figure S1b). Selected Dcp2-binding peptide sequences were appended to the N-terminus of the cysteine-free phage D1D2 domain of pIII with a C-terminal FLAG tag by PCR and cloned into pET28a between NcoI and HindIII sites, adding an additional C-terminal His<sub>6</sub> motif (“peptide-D1D2”). Alanine mutants of GST-Dcp2<sup>FL</sup> were generated using inverse PCR.

**Recombinant protein production.** All His<sub>6</sub>-tagged Dcp2 truncations and Dcp2<sup>FL</sup>-AP were purified by TALON resin (Clontech) as previously reported(Cohen et al., 2005; Liu et al., 2008). Briefly, Dcp2 expression was induced in BL21 Gold (DE3) cells with 0.4 mM isopropyl β-d-thiogalactoside (IPTG) at 20 °C overnight. Bacterial pellets were lysed by sonication in ice-cold lysis buffer A (50 mM Na<sub>2</sub>HPO<sub>4</sub>, pH 7.5, 600 mM NaCl, 300 mM urea, 10% glycerol, 1% Triton X-100) supplemented with 1 mg/mL lysozyme and DNaseI. The lysate was incubated with pre-equilibrated TALON beads at 4 °C for 1 h, and the resin was washed first with wash buffer A (50 mM Na<sub>2</sub>HPO<sub>4</sub>, pH 7.5, 600 mM NaCl, 10 mM imidazole, 300 mM urea, 0.5% Triton X-100) followed by wash buffer A<sub>0</sub> without Triton X-100 and urea. Bound protein was eluted with elution buffer (50 mM Na<sub>2</sub>HPO<sub>4</sub>, pH 7.5, 600 mM NaCl, 300 mM imidazole). Fractions containing Dcp2 were combined, concentrated and dialyzed against storage buffer (20 mM Tris, pH 7.2, 100 mM NaCl, 1 mM DTT, 1 mM MgCl<sub>2</sub>, 10% glycerol) for downstream applications. His<sub>6</sub>-BirA was expressed and purified as previously reported(Fairhead and Howarth, 2015).

**Phage selections with Dcp2<sup>FL</sup>-AP.** Three rounds of bio-panning were implemented with purified Dcp2<sup>FL</sup>-AP (2-5 μg) that was biotinylated by recombinant BirA(Fairhead and Howarth, 2015) and immobilized on streptavidin magnetic beads (NEB, S1420) as described previously(Rentero Rebollo and Heinis, 2013). In brief, isolated phage library and 50 μL streptavidin beads with or without immobilized Dcp2<sup>FL</sup>-AP were separately blocked with blocking buffer containing 3% (w/v) BSA and 0.3% Tween-20 and mixed for 30 min at room temperature. The beads were washed 8 times with 1 mL wash buffer (10 mM Tris-HCl, pH 7.4, 150 mM NaCl, 10 mM MgCl<sub>2</sub>, 1 mM CaCl<sub>2</sub>, 0.1% Tween-20) and twice with 1 mL buffer without Tween-20 before elution with 100 μL of 50 mM glycine, pH 2.2. The beads were transferred to different tubes every three washes to minimize non-specific phage binding to tubes. Eluted phages were neutralized with 50 μL of 1 M Tris-HCl, pH 8.0 and incubated with 25 mL of TG1 cells at OD<sub>600</sub> of 0.4 for 90 min at 37 °C without shaking. The cells were spun down, suspended in 1 mL of 2-YT and plated on large 2-YT/chloramphenicol plates. Plasmid DNA of >100 phage clones from the third round was sequenced (Genewiz, South Plainfield, NJ).

**GST pull-down assay.** Wild-type and mutant GST-Dcp2<sup>FL</sup> were expressed in Rosetta cells (DE3) in LB medium with 0.4 mM IPTG at 20 °C overnight. After cell lysis by sonication in lysis buffer A (50 mM Na<sub>2</sub>HPO<sub>4</sub>, pH 7.5, 600 mM NaCl, 300 mM urea, 10% glycerol, 1% Triton X-100) supplemented with lysozyme, DNase I and protease inhibitor cocktail (Roche), proteins were affinity purified sequentially using TALON matrix (Clontech) and glutathione agarose beads (GE Healthcare) according to manufacturer’s instruction. All peptide-D1D2-FLAG-His<sub>6</sub> fusion proteins were expressed in BL21 Gold (DE3) cells with 1 mM IPTG at 20 °C overnight and lysed in lysis buffer B (30 mM Na<sub>2</sub>HPO<sub>4</sub>, pH 7.4, 300 mM NaCl, 1 mM TCEP, 0.1% Triton X-100) supplemented with lysozyme, DNase I and protease inhibitor cocktail. All peptide-D1D2 fusions were purified on TALON resin and cyclized with TBMB as previously described(Rentero Rebollo and Heinis, 2013). GST-pull-downs using these purified proteins were then carried out in PBS by incubating mixtures of 0.4 μM GST-Dcp2<sup>FL</sup> and 4 μM cyclic peptide-D1D2-FLAG-His<sub>6</sub> on 25 μL glutathione beads at 4 °C overnight. The beads were washed twice with 5 bed volumes of PBS, 0.5% Tween 20 followed by four PBS washes. Bound proteins were eluted with 30 μL of 2x sample buffer and analyzed by SDS-PAGE followed by Western blotting.

**Chemical synthesis of bicyclic peptides.** All linear peptides (LP) were synthesized and derivatized at the C-terminus with amide and, for live cell imaging of peptide uptake, at the N-terminus with FITC through an Ahx linker by solid-phase chemistry (GenScript). All photo-cross-linkable linear peptides with N-term biotin were ordered from New England Peptide. For chemical cyclization, the crude linear peptides (0.5 mM) dissolved in degassed 80% (v/v) 20 mM NH<sub>4</sub>HCO<sub>3</sub>, 5 mM EDTA, pH 8.0 and 20% MeCN were each reacted with 1 mM TBMB at 30 °C for 90 min. The reaction product was purified by reverse phase HPLC using a semi-prep C18 column (Agilent) and gradient elution with a mobile phase composed of MeCN and 0.1% (v/v) aqueous formic acid solution at a flow rate of 1 mL min<sup>-1</sup>. The purified cyclic peptides (CP) were lyophilized and re-dissolved in degassed peptide storage buffer (50 mM Tris-HCl, pH 7.8, 150 mM NaCl) for downstream applications. Product was assessed by liquid chromatography-mass spectrometry (Agilent 6550A QTOF), with mass spectra obtained by electrospray in positive ion mode(Bird et al., 2008). Quantitation was achieved from the HPLC absorbance peak area (220 nm) for CP21 in all-L or all-D form using the uncyclized peptide with the same sequence, LP21 (GenScript), as the standard and by UV absorbance at 495 nm for FITC-labeled CP21 with an extinction coefficient of 77000 M<sup>-1</sup>cm<sup>-1</sup> (Dietrich et al., 2017).

**Isothermal Calorimetry (ITC).** Nano ITC (TA Instruments) was used to carry out the ITC analysis. All peptides used for the assay were lyophilized and re-dissolved in the same buffer containing 20 mM Tris-HCl (pH 7.2), 100 mM NaCl, and 1 mM MgCl<sub>2</sub>. The titrations were carried out at 293 K, with 100 μM of Dcp2<sup>1-349</sup> in the sample cell as titrate and 1 mM of CP21 in either isoform in the syringe as titrant. Data analysis was carried out using Nano Analyze provided by Nano ITC. All ITC data were fitted with a one-site binding model with baseline subtracted.

**In vitro photo-cross-linking.** Photo-cross-linking was performed in a microtiter plate on ice with purified His<sub>6</sub>-Dcp2<sup>1-349</sup> (1 μM) and each photo-CP (10 μM) in DPBS. The reaction mixture was pre-incubated at room temperature for 30 min prior to UV irradiation at 365 nm for 15 min. Samples were analyzed by SDS-PAGE followed by western blotting with an antibody to the Dcp2 or with Strep-HRP.

**Immunoprecipitation of RNA decapping complex.** HEK293T cells stably expressing FLAG-tagged DCP1A in 10 cm dishes were treated with either 2 μM CP21 or D-CP21 at 70% confluency for 18 h. Cells were then harvested and lysed on ice using 1 mL TBS with 1% Triton X-100 supplemented with Roche Complete protease inhibitor cocktail (Sigma-Aldrich). 10% cell lysate were saved for analysis of input. A 50 μL aliquot of pre-equilibrated anti-FLAG agarose beads (clone M2, Sigma-Aldrich) was added to each cell lysate and incubated at 4 °C for 1 h. The beads were washed 4 times with TBS-T and eluted with one bed volume of 3x FLAG peptide (Sigma-Aldrich) at a final concentration of 1 mg/mL in TBS. Beads were removed by centrifugation, and eluates were analyzed by SDS-PAGE followed by western blotting or subjected to on-bead trypsin digestion followed by liquid chromatography-tandem mass spectrometry (LC-MS/MS) proteomics analysis.

**Photo-cross-linking in cell lysates and proteomics (Target ID).** HEK293T cells were transiently transfected with pcDNA3-FLAG-Dcp2<sup>FL</sup>. After 24 h of transfection, cells were harvested and lysed in radioimmunoprecipitation assay (RIPA) buffer (10 mM Tris-HCl, pH 7.4, 1% Triton X-100, 0.1% sodium deoxycholate, 0.1% SDS, 10 mM NaCl) supplemented with protease inhibitors (Roche). 300  $\mu$ L of whole cell lysate diluted to 1 mg/mL in DPBS was added to each reaction mixture. Photo-CP-3 was then added at 50  $\mu$ M concentration, with or without 250  $\mu$ M CP21 as competitor. Reaction mixtures were incubated at 4 °C with rotating for 1 h, followed by UV crosslinking (365 nm, 23 W) on ice for 1 h. 10  $\mu$ L samples were taken and subjected to SDS-PAGE followed by western blotting analysis. The remaining samples were supplemented with 3% BSA and loaded on 60  $\mu$ L streptavidin magnetic beads (NEB) pre-washed with RIPA buffer, followed by 1 h incubation at room temperature. The beads were washed twice with 1 mL RIPA buffer, once with 1 M KCl, once with 0.1 M sodium carbonate, once with 2 M urea, and twice with RIPA buffer. On-bead trypsin digestion and ultramicrospin clean-up were performed before run on a Thermo Q-Exactive Plus instrument as previously described (Cao et al., 2020; D'Lima et al., 2017). Mass spectra were analyzed using Mascot (Perkins et al., 1999) against uniprot\_human database, and label-free quantitation (LFQ) was carried out using MaxQuant (Cox and Mann, 2008) followed by Perseus (Tyanova et al., 2016).

**Cellular thermal shift assay (CETSA).** HEK293T cells in 100 mm dishes were treated with either 2  $\mu$ M CP21 or its all-D form (D-CP21) or the same volume of vehicle (peptide storage buffer, 50 mM Tris-HCl, pH 7.8, 150 mM NaCl) at 70% confluency. After 18 h, cells were harvested, washed twice with DPBS and resuspended in 1 mL PBS containing one tablet of protease inhibitors (Roche). Each cell suspension was distributed into ten PCR tubes and heated to temperatures ranging from 45 to 65 °C for 3 min using an MJ Research PTC-200 PCR thermal cycler, followed by incubation at room temperature for 3 min. The samples were freeze-thawed twice using liquid nitrogen, vortexed briefly and spun down at 20,000 g for 20 min at 4 °C. The supernatant was then removed and analyzed by SDS-PAGE followed by western blotting (Jafari et al., 2014). To generate the melting curves shown in Figure 2d and Figure S5, bands corresponding to each protein were first quantified in Fiji (Schindelin et al., 2012) and normalized to the beta-actin bands. The resulting relative intensity was normalized by setting the highest and lowest value for each protein to 100 and 0%, respectively. Data were then analyzed using Boltzmann Sigmoid equation in GraphPad Prism (Jafari et al., 2014).

**Generation of stable rescue cell lines.** DCP2 KO HEK293T cells were co-transfected with wild-type or alanine mutant Dcp2<sup>FL</sup> cloned into pLJM1, along with pMD2.G and psPAX2. Media containing viruses was harvested 48 h after transfection, aliquoted and kept at -80 °C prior to transduction. Stable cell lines were generated by transducing with diluted virus stock (1:3) at around 70% cell confluency for 48 h. Cells were harvested 48 h after puromycin selection, and expression level of Dcp2 was validated by western blotting.

**Cell-based RNA decay assay.** DCP2 KO or wild-type (WT) HEK293T cells were cultured in 6-well plates and treated with either 2  $\mu$ M CP21 or D-CP21 or the same volume of vehicle at 50–70% confluency for 18 h. Alternatively, respective cells were cultured to a confluency of 80–90% before experiments. Cells were harvested on ice at the indicated time points after transcriptional arrest by actinomycin D (5  $\mu$ g/mL). Total RNA was isolated with RNeasy Mini kit (Qiagen) or TRIzol (Invitrogen) following the manufacturer's instructions, followed by DNase I (NEB) treatment. RNA levels were quantified using reverse-transcribed cDNA from the same amount of input RNAs by real-time PCR using iTaq Universal SYBR Green Supermix (Bio-Rad) based on a comparative Ct method as described previously (Blewett et al., 2011). In brief, RNA amounts remaining at each time point relative to time = 0 h were calculated using  $2^{-\Delta C_t}$ , where  $\Delta C_t = C_t(t) - C_t(0)$  (time point) (Blewett et al., 2011). Alternatively, relative RNA level was normalized to  $\beta$ -actin before subjected to analysis by comparative Ct method (Schmittgen and Livak, 2008). All data points were then fit into an exponential decay model. Two-tailed *t*-test or analysis of variance (ANOVA) was performed using Excel, GraphPad Prism 7 or Origin 2018. Equal variance between samples was established using an *F*-test, and multiple comparisons were performed with Dunnett's test following one-way ANOVA. Previously reported primers were used for *RRP41* (Li et al., 2008) and *HOXA13* (Luo et al., 2020). Forward and reverse primers used for other genes were as follows (Gene-Fwd/-Rev): PLBD2-Fwd: 5' GGCCCTTCGAGTATGAAGTC 3'; PLBD2-Rev: 5' TCCTGCATCCACTCTAGGTTG 3'; RFX7-Fwd: 5' ACTGGAGATGGGTGGAAGG 3'; RFX7-Rev: 5' AGACGGCAAGCAGAAGAGAT 3'; ARHGAP32-Fwd: 5' CCATGCCTGGAGGTTTAGTT 3'; ARHGAP32-Rev: 5' CTTCAGACTCCAACCAGAAGAC 3'; PAX6-Fwd: 5' CTCTCACCAGCAACTCCTTT 3'; PAX6-Rev: 5' CCCTTTATGAGGCATCCTTTCT 3'; SRSF12-Fwd: 5' AGAAATAGGAGGCGGTCAGA 3'; SRSF12-Rev: 5' TTGACTGCCTTGCTGAGGTA 3'; ANKRD13A-Fwd: 5' TGCACCTCCTAGTCTGGAAAA 3'; ANKRD13A-Rev: 5' AGATGCAATAATGTTCGACCTCG 3'; ERGIC2-Fwd: 5' GGACCATAACACAAGCATGACTA 3'; ERGIC2-Rev: 5' TCTCTACATAGCTCTCAGGAACC 3'; ERGIC2-Splint: 5' GGGTCGCCGGGGCTCATCAAAGCCAGCAAACGCAGTGTTTCATTC 3'.

**P-body imaging using confocal microscopy.** HEK293T cells were grown on fibronectin-coated glass coverslips in a 48-well plate to 50% confluency and treated with 2  $\mu$ M CP21 or D-CP21 or the same volume of vehicle for 18 h. Cells were fixed with 10% neutral buffered formalin (Fisher Scientific), permeabilized with methanol at -20 °C, and blocked with blocking buffer (3% BSA in DPBS) for 1 h at room temperature. Cells were stained with rabbit anti-DCP1A (Fenger-Gron et al., 2005) at a 1:1000 dilution in blocking buffer overnight at 4 °C, followed by 3x PBS washes. Goat anti-rabbit Alexa Fluor 568 was applied at a 1:1000 dilution in blocking buffer for 1 to 4 h at room temperature in dark, with 3 subsequent PBS washes. Cells were post-fixed with 10% buffered formalin, stained with DAPI, and imaged by laser scanning confocal microscopy (Leica TCS SP8) with PL APO 63x/1.40 oil, CS2 and PL APO 100x/1.44 oil, CORR CS. P-body numbers were counted using ImageJ as described previously (Nissan and Parker, 2008).

**Live cell imaging.** HEK293T cells were grown on glass coverslips in a 48-well plate to 70% confluency and treated with 3  $\mu$ M FITC-Ahx-CP21, FITC-labeled all-D CP21 (FITC-Ahx-D-CP21) or the same volume of vehicle for 5 h. The growth medium was aspirated immediately before imaging. The cells were washed three times with pre-warmed PBS and covered in PBS for immediate room-temperature analysis by confocal microscopy with HCX PL APO 100x/1.44 oil objective (Leica TCS SP8).

**TimeLapse-seq.** TimeLapse-seq experiment was performed as previously described (Luo et al., 2020). Briefly, wild-type (WT) HEK293T and DCP2 KO cells were pre-treated with 2  $\mu$ M CP21 or D-CP21 (5 h) in duplicate followed by incubation with 500  $\mu$ M sU for 2 h, and a single replicate control per cell line was not treated with sU. Total RNA was isolated from cell pellets using TRIzol reagent, followed by phenol-chloroform extraction and isopropanol precipitation supplemented with 50  $\mu$ M DTT. After washing twice with 75% ethanol, dried RNA pellet was resuspended in nuclease-free water and treated with Turbo DNase to remove genomic DNA. RNA was isolated using

RNAclean beads, treated with TimeLapse chemistry (2,2,2-trifluoroethylamine and sodium periodate) and purified as previously described (Schofield et al., 2018). Purified recoded RNA was then sequenced using the mammalian pico-input SMARTer stranded Total RNA-seq kit v2. Paired-end 100 nt or 150 nt RNA sequencing was performed using an Illumina HiSeq-4000 or Novaseq. For data analysis, TimeLapse-seq reads were trimmed and aligned to mature RNA isoforms, and mutation calling was performed as described previously (Schofield et al., 2018). Assignment of new and old sequencing reads using per-read mutation cutoffs was performed as described in Luo et al. 2020 (Luo et al., 2020). Old and new read counts per gene were normalized per sample based on total RNA counts using EdgeR. Log(fold change) analysis was performed using DESeq2 on total, new, and old RNA counts, with scale factors from total RNA input into new and old RNA analyses. Change in RNA synthesis and degradation rates were determined using the following equations:  $k_{deg} = -\log(1-f_{new}) / t$ ;  $k_{syn} = [RNA] * k_{deg}$ , where  $f_{new}$  is the fraction of new RNA and  $[RNA]$  is the normalized total RNA read count per gene.

**Quantitative splinted ligation RT-PCR (qSL-RT-PCR).** The detection of decapped *HOXA13* RNA by qSL-RT-PCR was performed in *XRNI* KO HEK293T cells as previously described (Luo et al., 2020). In brief, *XRNI* KO cells were cultured in 6-well plates and subjected to specified treatment (CP21, D-CP21, or vehicle) for 18 h. Actinomycin D (5  $\mu$ g/mL) was added to stop transcription, and cells were harvested on ice at the indicated time points after transcriptional arrest. Total RNA was isolated with the RNeasy Mini kit, and 10  $\mu$ g total RNA was mixed with 10 pmol of each splint oligonucleotide and 30 pmol of anchor RNA (5'-GCUGAUGGCGAUGAAUGAACACUGCGUUUGCUGGCUUUGAUG-3'). The oligos were annealed by sequential incubation for 5 min from 70 °C to 60 °C to 42 °C and to 25 °C, followed by the ligation step with 2  $\mu$ L T4 DNA ligase (NEB) at 16 °C overnight. 20 U RNasin Plus (Promega) was included to prevent RNA degradation. 2  $\mu$ L DNase I (NEB) was then added to digest genomic DNA for 1 h at 37 °C. The RNA was precipitated with 0.3 M sodium acetate (pH 5.2) and 2.5 volume of ethanol at -20 °C overnight, washed with 70% ethanol and resuspended in 15  $\mu$ L of DEPC-treated water. cDNA was synthesized from 2  $\mu$ g of the ligated RNA with iScript kit (Bio-rad). Total RNA and splinted ligation product level was then quantified by real-time PCR using gene specific Fwd/Rev primers and Anchor Fwd/Rev primers (Luo et al., 2020). A  $\Delta\Delta C_t$  method was used to determine the relative level of decapped RNA (Blewett et al., 2011), and the amounts of total RNA remaining at each time point relative to time = 0 h were calculated from  $2^{\Delta C_t}$  using  $C_t$  (t = 0 h) as the reference value. Analysis of variance (ANOVA) was performed using Excel, GraphPad Prism 7 or Origin 2018. Equal variance between samples was established using an *F*-test, and multiple comparisons were performed with Dunnett's test following one-way ANOVA.

## SUPPLEMENTAL INFORMATION

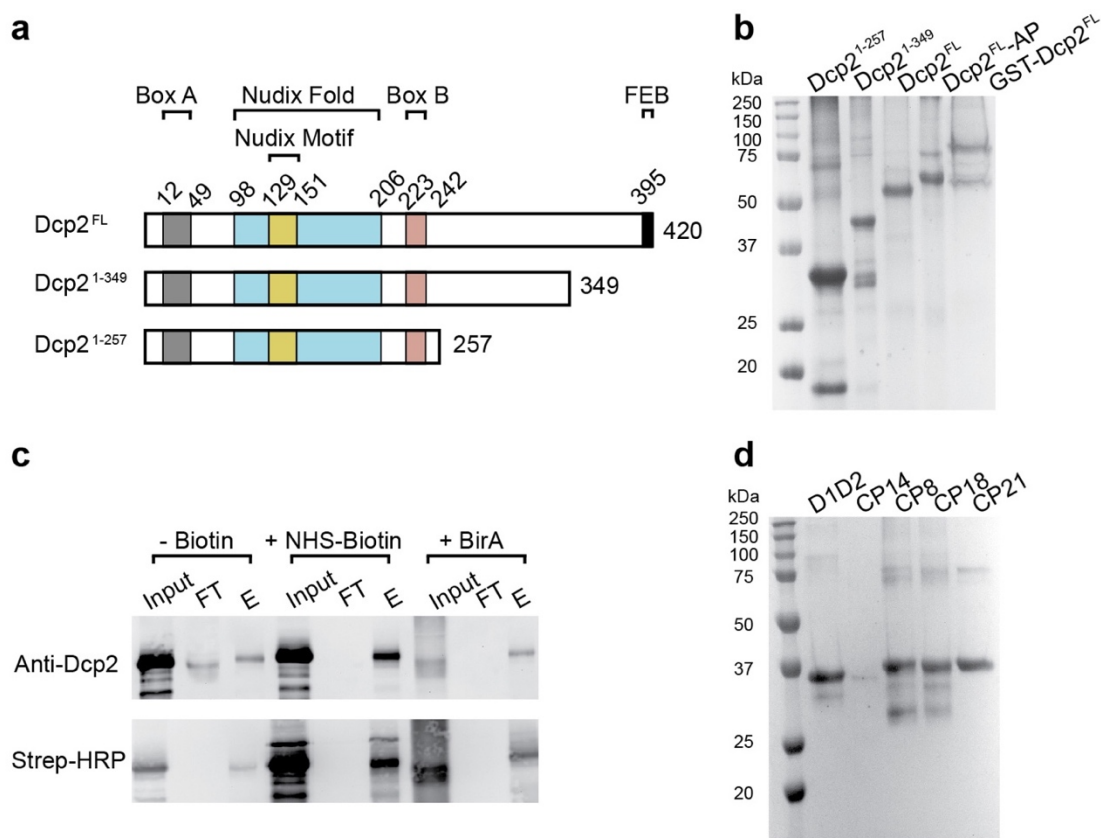


**Figure S1. Purification and biotinylation of fusion proteins for affinity selection and pull-downs (related to Figure 1-2).** (a) Schematic representation of full-length human Dcp2 (Dcp2<sup>FL</sup>) and two previously reported catalytically active Dcp2 truncations (Piccirillo et al., 2003). The three conserved functional motifs, Box A (gray), catalytic Nudix motif (yellow) within the Nudix fold (cyan), and Box B (pink) are highlighted. The short C-terminal disordered phenylalanine-rich EDC4 binding (FEB) motif responsible for EDC4 binding (Chang et al., 2014) is shown in black. All proteins contain a C-terminal His<sub>6</sub> tag for purification. For some experiments, AviTag peptide (AP) was added by inverse PCR to the C-terminus, and a GST fusion construct was appended to the N-terminus (see Methods). Numbers represent amino acid positions. (b) SDS-PAGE analysis of all Dcp2 truncations and tagged full-length proteins used in this study (12% polyacrylamide gel stained with Coomassie blue). Lower bands from Dcp2 truncations represent products of degradation. (c) Confirmation of *in vitro* BirA biotinylation of Dcp2<sup>FL</sup>-AP by streptavidin pull-down assay. Aliquots of 1 bead volume of each biotinylation reaction were mixed with 20  $\mu$ L of streptavidin magnetic beads and incubated at room temperature for 30 min. The bound fractions were eluted by boiling in SDS sample buffer for 20 min and loaded on 10% acrylamide gel together with the supernatant (FT) and input for analysis by western blot. (d) SDS-PAGE analysis of FLAG-tagged D1D2 domain of phage protein pIII and the four TBMB-cyclized peptide (CP)-D1D2 fusions used for the pull-down experiment in **Figure 2b**. The proteins were stained with Coomassie blue.

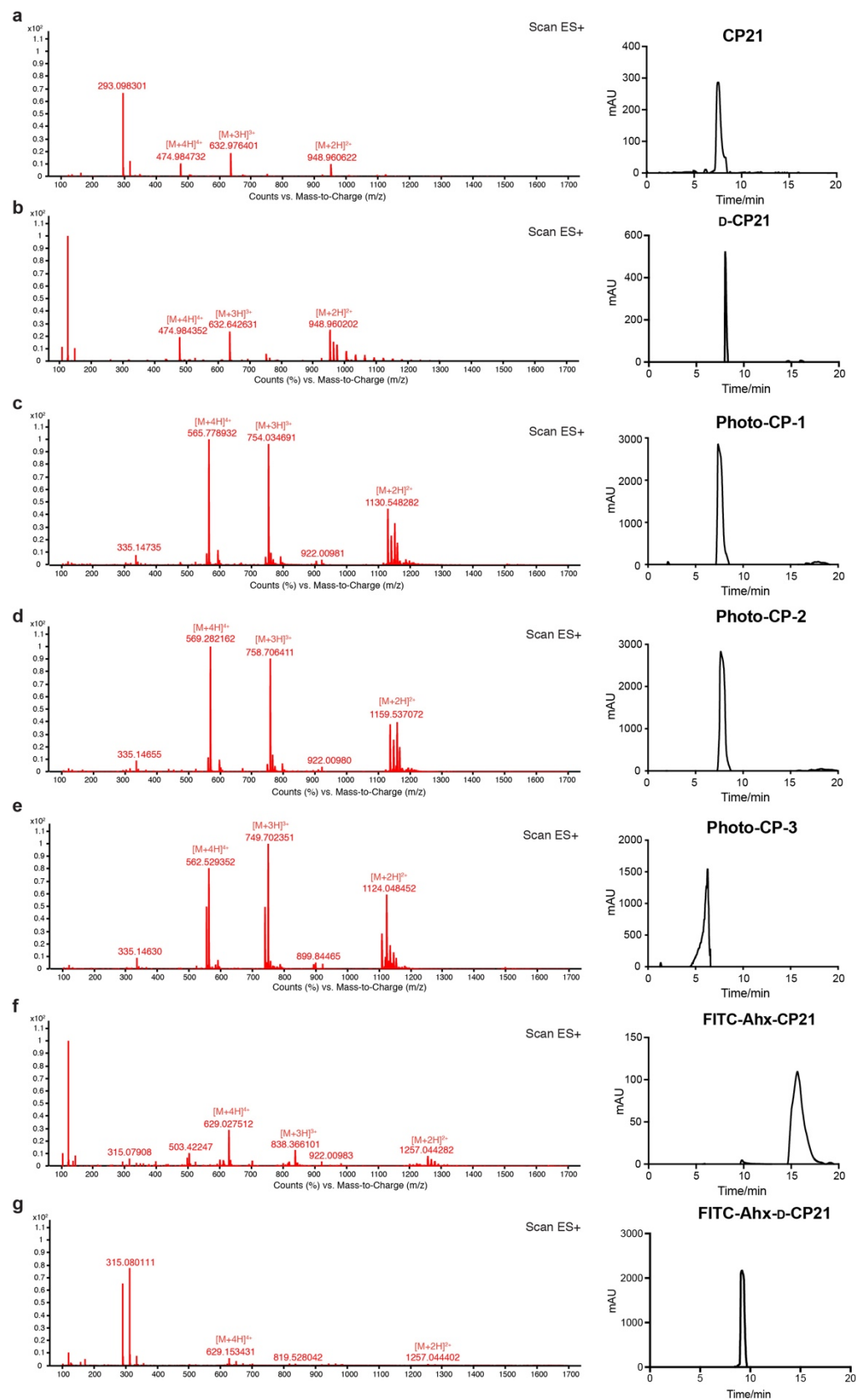


**Figure S2. LC/MS and HPLC traces for all chemically synthesized peptides used in this study (related to Figure 2-3).** (a) CP21, (b) all-D CP21 (D-CP21), (c-e) Photo-cross-linkable CP21 analogue (Photo-CP-1 to -3), (f) FITC-Ahx-CP21 and (g) all-D FITC-Ahx-CP21 (FITC-Ahx-D-CP21) in storage buffer were diluted 1/50 in ddH<sub>2</sub>O for liquid chromatography-mass spectrometry (LC/MS) analysis (left panels) to confirm purified product masses. HPLC traces (right panels) show purity.

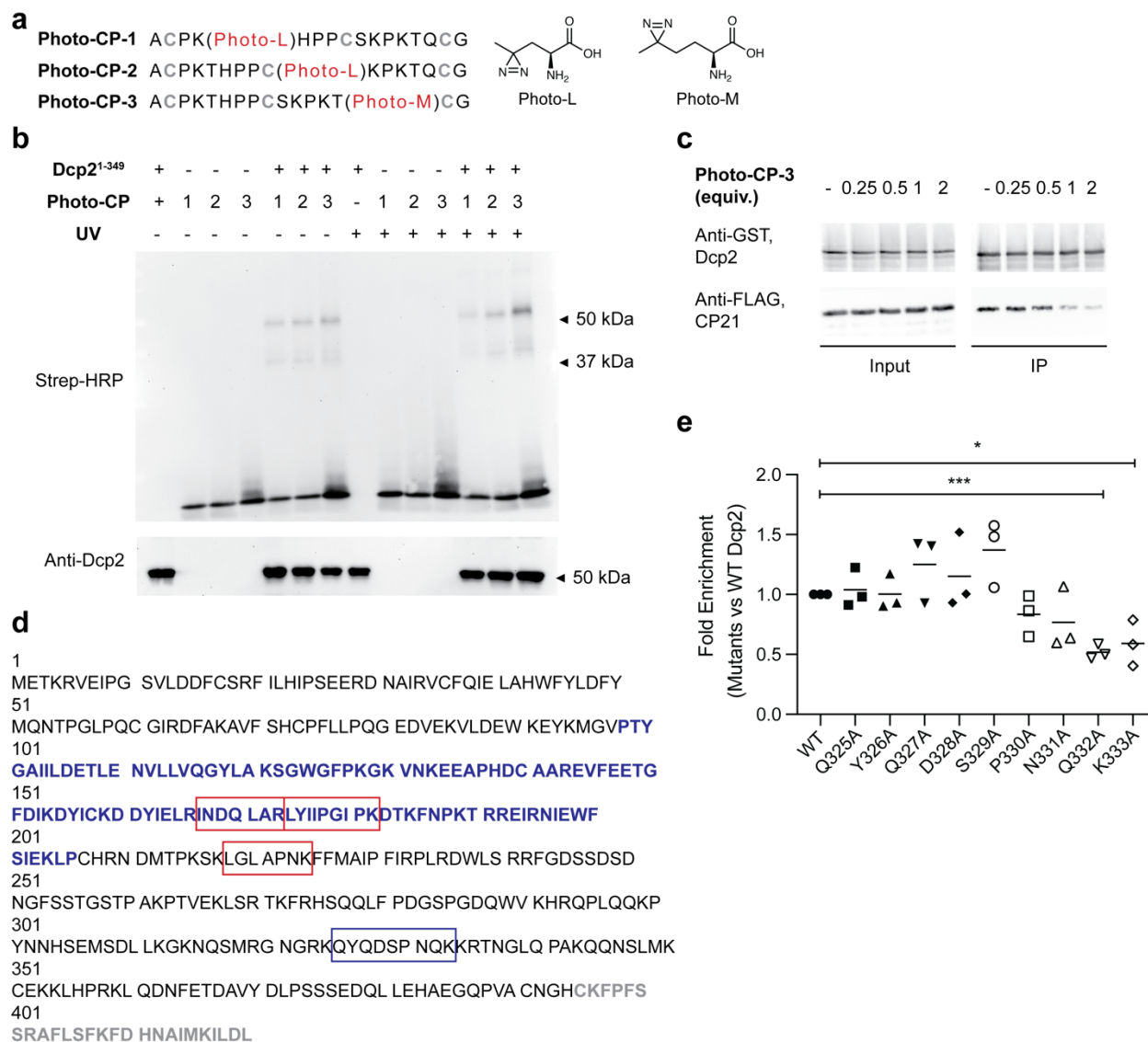


**Figure S3. A segment of the C-terminus disordered region of Dcp2 is involved in CP21 binding (related to Figure 2-3).** (a) Design of photo-cross-linkable CP21 probes. L-Photo-Methionine (Photo-M) or L-Photo-Leucine (Photo-L) were incorporated into CP21 during synthesis at three residues not conserved from prior selection result. (b) Photo-cross-linking of each CP21 probe with purified Dcp2<sup>1-349</sup> at 365 nm. A higher molecular weight cross-linked product was observed near the molecular weight of Dcp2. (c) Pulldown of FLAG epitope-tagged CP21-D1D2 fusion proteins (CP21-D1D2-FLAG) with recombinant GST-tagged wild-type full length Dcp2 (GST-Dcp2<sup>FL</sup>) in the absence or presence of increasing amount of Photo-CP-3. Stoichiometry of Photo-CP-3 relative to CP21-D1D2-FLAG (equiv.) is indicated at the top. (d) Respective regions of Dcp2 photo-cross-linked to Photo-CP-3. Boxes indicated the four fragments consistently missing from UV irradiated samples vs unirradiated control are emphasized in boxes (red, observed in at least two out of three of the unirradiated control replicates; blue, additionally validated by *in vitro* pull-down). Experiments were performed three times independently. The Nudix domain are highlighted in blue and the FEB motif in grey. (e) Alanine scanning mutagenesis of Dcp2 between amino acid residues 325 and 333 was performed to identify residues directly interacting with CP21. Wild-type GST-Dcp2<sup>FL</sup> or the indicated mutants were separately co-incubated with 10-fold molar excess of the CP21-D1D2-FLAG, with CP21-D1D2-FLAG alone as a negative control, and GST pull-down was performed prior to western blot detection. Lines from the scatter plot indicate the mean value of CP21-D1D2-FLAG enrichment using each Dcp2 mutant comparing to the wild-type protein.

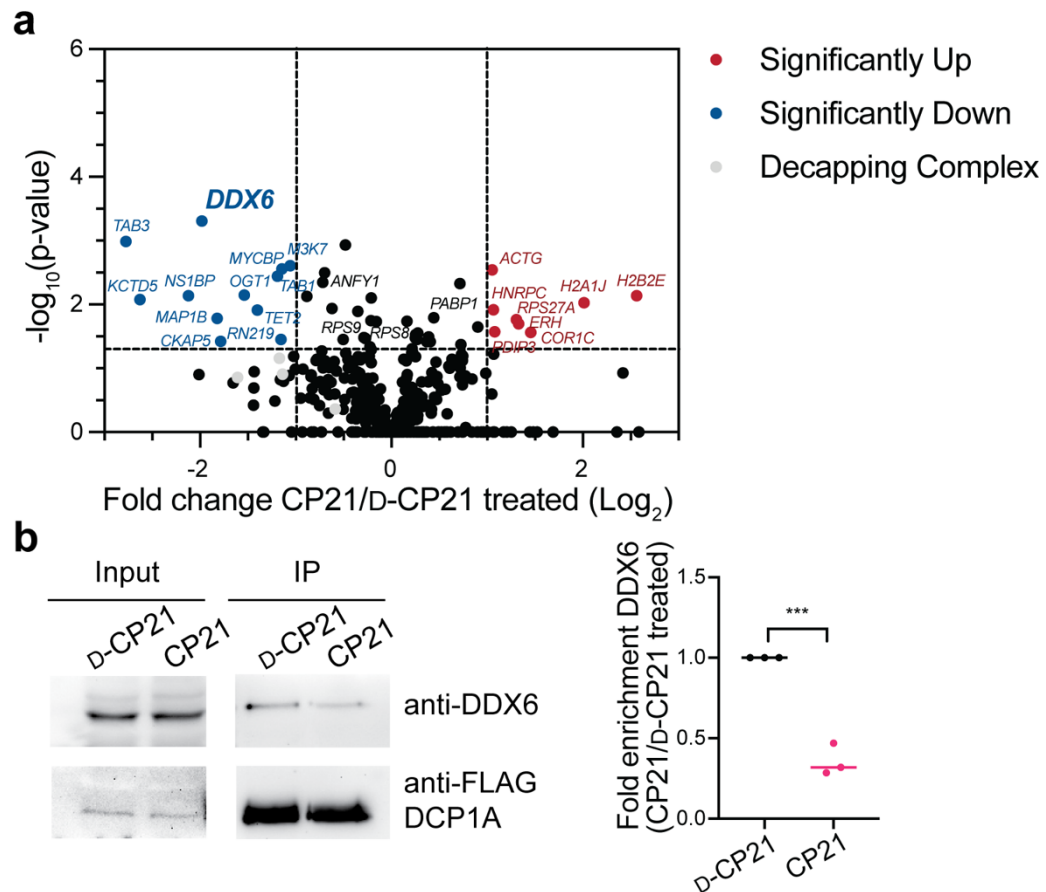


**Figure S4. CP21 regulates the interaction between RNA decapping factors (related to Figure 3 and Figure S3).** RNA decapping complexes were purified from HEK293T cells stably expressing FLAG-DCP1A after pre-treatment with CP21 vs D-CP21 (2  $\mu$ M, 18 h). Mass spectrometry analysis was performed to identify difference in the composition of immunopurified decapping complex (a). The most depleted protein, DDX6, in CP21 vs D-CP21-treated groups was further validated by western blotting (b). Data represent three biological replicates. Lines from the scatter plot (b, right) indicate the mean value of DDX6 band intensity normalized to that of DCP1A probed using anti-FLAG.



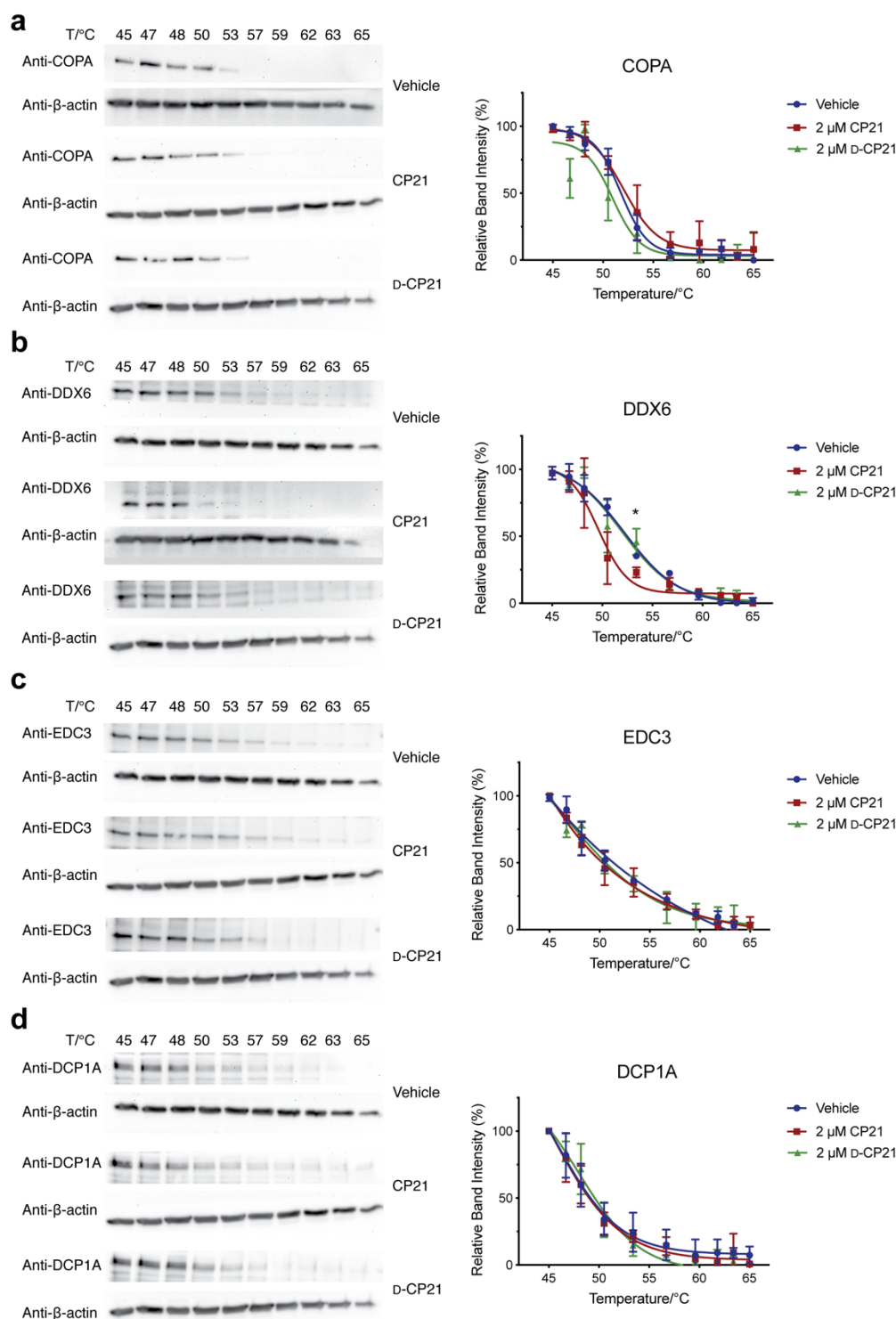


**Figure S5. Monitoring CP21-engaged proteins using CETSA (related to Figure 3 and Figure S4).** Representative western blot analysis of thermal stability (left) and CETSA melt curves (right) for a potential off-target of CP21, COPA (a), and decapping complex components, DDX6, EDC3 and DCP1A (b-d) in the presence and absence of 2 μM CP21 or D-CP21 in intact HEK293T cells transiently transfected with FLAG-NUDT16. Significant difference in relative DDX6 intensity at 53 °C was analyzed by one-way ANOVA. Data are plotted as means  $\pm$  s.d.;  $n = 3$  biological replicates. P-values (with Dunnett's test) are denoted by asterisks; (\*)  $p < 0.05$ .

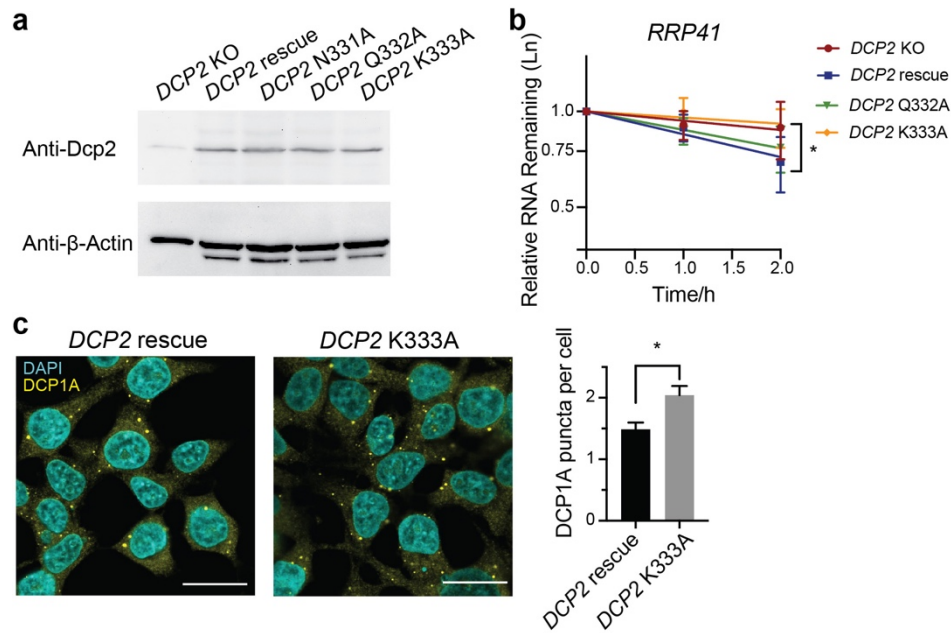


**Figure S6. K333 is important for CP21 binding and human Dcp2 function (related to Figure 4 and Figure S3).** (a) Analysis of Dcp2 expression in *DCP2* rescue HEK293T and mutant complementation cell lines by western blot. (b) *RRP41* RNA decay curves from *DCP2* knockout (KO) HEK293T cells versus *DCP2* rescue or two non-CP21-interacting mutant Dcp2 complementation cell lines. The levels of *RRP41* RNA remaining following actinomycin D treatment at indicated time points relative to  $t = 0$  h were determined by qRT-PCR. Significance was analyzed by ANOVA linear regression. Number of biological repeats:  $n=4$ . P-values with Dunnett's test are denoted by asterisks; (\*)  $p<0.05$ . (c) P-body numbers in *DCP2* rescue versus *DCP2* K333A complementation cell line. Fixed cells were stained with antibodies detecting DCP1A, a P-body marker. At least 300 cells from six fields of view were used to quantitate average P-bodies per cell in each condition. P-body numbers were counted using ImageJ (see Methods). Data represent mean values  $\pm$  s.e.m. Significance was evaluated with two-tailed  $t$ -test; (\*)  $p<0.05$ . Scale bars, 25  $\mu$ m.

**Table S1. Genes specifically stabilized by CP21 vs D-CP21 via Dep2**

<b>Genes</b>	<b>Gene Descriptions</b>
<b>ABR</b>	<i>Homo sapiens</i> active BCR-related
<b>AES</b>	<i>Homo sapiens</i> amino-terminal enhancer of split
<b>AGBL5</b>	<i>Homo sapiens</i> ATP/GTP binding protein like 5
<b>ALG10</b>	<i>Homo sapiens</i> alpha-1,2-glucosyltransferase
<b>ANKRD13A</b>	<i>Homo sapiens</i> ankyrin repeat domain 13A
<b>ARFRP1</b>	<i>Homo sapiens</i> ADP ribosylation factor related protein 1
<b>ARHGAP32</b>	<i>Homo sapiens</i> Rho GTPase activating protein 32
<b>ARMCX3</b>	<i>Homo sapiens</i> armadiollo repeat containing, X-linked 3
<b>ATP11A</b>	<i>Homo sapiens</i> ATPase phospholipid transporting 11A
<b>BCS1L</b>	<i>Homo sapiens</i> BCS1 homolog, ubiquinol-cytochrome c reductase complex chaperone
<b>BUB1B</b>	<i>Homo sapiens</i> BUB1 mitotic checkpoint serine/threonine kinase B
<b>C18orf21</b>	<i>Homo sapiens</i> chromosome 18 open reading frame 21
<b>CABYR</b>	<i>Homo sapiens</i> calcium binding tyrosine phosphorylation regulated
<b>CARHSP1</b>	<i>Homo sapiens</i> calcium regulated heat stable protein 1
<b>CCT8</b>	<i>Homo sapiens</i> chaperonin containing TCP1 subunit 8
<b>CEP290</b>	<i>Homo sapiens</i> centrosomal protein 290
<b>CHUK</b>	<i>Homo sapiens</i> conserved helix-loop-helix ubiquitous kinase
<b>COPS2</b>	<i>Homo sapiens</i> COP9 signalosome subunit 2
<b>DDX17</b>	<i>Homo sapiens</i> DEAD-box helicase 17
<b>DDX39B</b>	<i>Homo sapiens</i> DEAD-box helicase 39B
<b>EML4</b>	<i>Homo sapiens</i> echinoderm microtubule associated protein like 4
<b>EPPK1</b>	<i>Homo sapiens</i> epiplakin 1
<b>ERGIC2</b>	<i>Homo sapiens</i> ERGIC and golgi2
<b>ERO1A</b>	<i>Homo sapiens</i> endoplasmic reticulum oxidoreductase 1 alpha
<b>EXD2</b>	<i>Homo sapiens</i> exonuclease 3'-5' domain containing 2
<b>FAM168B</b>	<i>Homo sapiens</i> family with sequence similarity 168 member B
<b>FANCB</b>	<i>Homo sapiens</i> Fanconi anemia complementation group B
<b>FNTA</b>	<i>Homo sapiens</i> farnesyltransferase, CAAX box, alpha
<b>FUNDC2</b>	<i>Homo sapiens</i> FUN14 domain containing 2
<b>GIN5</b>	<i>Homo sapiens</i> GINS complex subunit 4
<b>GRHPR</b>	<i>Homo sapiens</i> glyoxylate and hydroxypyruvate reductase
<b>HARS</b>	<i>Homo sapiens</i> histidyl-tRNA synthetase

<b>HCCS</b>	<i>Homo sapiens</i> holocytochrome c synthase
<b>HNRNPA0</b>	<i>Homo sapiens</i> heterogeneous nuclear ribonucleoprotein A0
<b>HS6ST1P1</b>	<i>Homo sapiens</i> heparan sulfate 6-O-sulfotransferase 1 pseudogene 1
<b>HSD17B7</b>	<i>Homo sapiens</i> hydroxysteroid 17-beta dehydrogenase 7
<b>ILKAP</b>	<i>Homo sapiens</i> ILK associated serine/threonine phosphatase
<b>INPP5A</b>	<i>Homo sapiens</i> inositol polyphosphate-5-phosphatase A
<b>JOSD1</b>	<i>Homo sapiens</i> Josephin domain containing 1
<b>KHNYN</b>	<i>Homo sapiens</i> KH and NYN domain containing
<b>KLHL17</b>	<i>Homo sapiens</i> kelch like family member 17
<b>LMF2</b>	<i>Homo sapiens</i> lipase maturation factor 2
<b>LSM6</b>	<i>Homo sapiens</i> LSM6 homolog, U6 small nuclear RNA and mRNA degradation associated
<b>MBD1</b>	<i>Homo sapiens</i> methyl-CpG binding domain protein 1
<b>MEGF8</b>	<i>Homo sapiens</i> multiple EGF like domains 8
<b>MMACHC</b>	<i>Homo sapiens</i> methylmalonic aciduria (cobalamin deficiency) cblC type, with homocystinuria
<b>MOCS2</b>	<i>Homo sapiens</i> molybdenum cofactor synthesis 2
<b>MRPL14</b>	<i>Homo sapiens</i> mitochondrial ribosomal protein L14
<b>MSH3</b>	<i>Homo sapiens</i> mutS homolog 3
<b>NBPF14</b>	<i>Homo sapiens</i> neuroblastoma breakpoint family member 14
<b>NOL4L</b>	<i>Homo sapiens</i> nucleolar protein 4 like
<b>ODC1</b>	<i>Homo sapiens</i> ornithine decarboxylase 1
<b>OGFR</b>	<i>Homo sapiens</i> opioid growth factor receptor
<b>PAGR1</b>	<i>Homo sapiens</i> PAXIP1 associated glutamate rich protein 1
<b>PARS2</b>	<i>Homo sapiens</i> prolyl-tRNA synthetase 2, mitochondrial
<b>PAX6</b>	<i>Homo sapiens</i> paired box 6
<b>PDHB</b>	<i>Homo sapiens</i> pyruvate dehydrogenase (lipoamide) beta
<b>PEPD</b>	<i>Homo sapiens</i> peptidase D
<b>PET100</b>	<i>Homo sapiens</i> PET100 homolog
<b>PIAS2</b>	<i>Homo sapiens</i> protein inhibitor of activated STAT2
<b>PLEKHJ1</b>	<i>Homo sapiens</i> pleckstrin homology domain containing J1
<b>PPP4R3A</b>	<i>Homo sapiens</i> protein phosphatase 4 regulatory subunit 3A
<b>PSMF1</b>	<i>Homo sapiens</i> proteasome inhibitor subunit 1
<b>PUSL1</b>	<i>Homo sapiens</i> pseudouridylate synthase-like 1
<b>RAVER1</b>	<i>Homo sapiens</i> ribonucleoprotein, PTB binding 1

<b>RFX7</b>	<i>Homo sapiens</i> regulatory factor X7
<b>RIMKLA</b>	<i>Homo sapiens</i> ribosomal modification protein rimK like family member A
<b>RP11-295P9.3</b>	<i>Homo sapiens</i> pre-mRNA processing factor 31 (PRPF31)
<b>RPAP2</b>	<i>Homo sapiens</i> RNA polymerase II associated protein 2
<b>SAPCD2</b>	<i>Homo sapiens</i> suppressor APC domain containing 2
<b>SDHB</b>	<i>Homo sapiens</i> succinate dehydrogenase complex iron sulfur subunit B
<b>SIAH1</b>	<i>Homo sapiens</i> siah E3 ubiquitin protein ligase 1
<b>SLC35A4</b>	<i>Homo sapiens</i> solute carrier family 35 member A4
<b>SMAP1</b>	<i>Homo sapiens</i> small ArfGAP1
<b>SOCS6</b>	<i>Homo sapiens</i> suppressor of cytokine signaling 6
<b>SRSF12</b>	<i>Homo sapiens</i> serine and arginine rich splicing factor 12
<b>SRSF7</b>	<i>Homo sapiens</i> serine and arginine rich splicing factor 7
<b>STAG3L2</b>	<i>Homo sapiens</i> stromal antigen 3-like 2
<b>STK25</b>	<i>Homo sapiens</i> serine/threonine kinase 25
<b>TES</b>	<i>Homo sapiens</i> testin LIM domain protein
<b>TFDP2</b>	<i>Homo sapiens</i> transcription factor Dp-2
<b>TPM1</b>	<i>Homo sapiens</i> tropomyosin 1 (alpha)
<b>TRAF4</b>	<i>Homo sapiens</i> TNF receptor associated factor 4
<b>TRIM8</b>	<i>Homo sapiens</i> tripartite motif containing 8
<b>TSPAN33</b>	<i>Homo sapiens</i> tetraspanin 33
<b>UGP2</b>	<i>Homo sapiens</i> UDP-glucose pyrophosphorylase 2
<b>UQCR10</b>	<i>Homo sapiens</i> ubiquinol-cytochrome c reductase, complex III subunit X
<b>ZDHHC3</b>	<i>Homo sapiens</i> zinc finger DHHC-type containing 3
<b>ZNF180</b>	<i>Homo sapiens</i> zinc finger protein 180
<b>ZNF432</b>	<i>Homo sapiens</i> zinc finger protein 432
<b>ZRANB3</b>	<i>Homo sapiens</i> zinc finger RANBP2-type containing 3

---

## REFERENCES

- Aizer, A., Kalo, A., Kafri, P., Shrager, A., Ben-Yishay, R., Jacob, A., Kinor, N., and Shav-Tal, Y. (2014). Quantifying mRNA targeting to P-bodies in living human cells reveals their dual role in mRNA decay and storage. *J Cell Sci* 127, 4443-4456.
- Angelini, A., Cendron, L., Chen, S., Touati, J., Winter, G., Zanotti, G., and Heinis, C. (2012). Bicyclic peptide inhibitor reveals large contact interface with a protease target. *ACS Chem Biol* 7, 817-821.
- Arribas-Layton, M., Wu, D., Lykke-Andersen, J., and Song, H. (2013). Structural and functional control of the eukaryotic mRNA decapping machinery. *Biochim Biophys Acta* 1829, 580-589.
- Behm-Ansmant, I., Rehwinkel, J., Doerks, T., Stark, A., Bork, P., and Izaurralde, E. (2006). mRNA degradation by miRNAs and GW182 requires both CCR4:NOT deadenylase and DCP1:DCP2 decapping complexes. *Genes Dev* 20, 1885-1898.
- Bird, G.H., Bernal, F., Pittler, K., and Walensky, L.D. (2008). Synthesis and biophysical characterization of stabilized alpha-helices of BCL-2 domains. *Methods Enzymol* 446, 369-386.
- Blewett, N., Collier, J., and Goldstrohm, A. (2011). A quantitative assay for measuring mRNA decapping by splinted ligation reverse transcription polymerase chain reaction: qSL-RT-PCR. *RNA* 17, 535-543.
- Cao, X., Khitun, A., Na, Z., Dumitrescu, D.G., Kubica, M., Olatunji, E., and Slavoff, S.A. (2020). Comparative Proteomic Profiling of Unannotated Microproteins and Alternative Proteins in Human Cell Lines. *J Proteome Res* 19, 3418-3426.
- Chang, C.T., Bercovich, N., Loh, B., Jonas, S., and Izaurralde, E. (2014). The activation of the decapping enzyme DCP2 by DCP1 occurs on the EDC4 scaffold and involves a conserved loop in DCP1. *Nucleic Acids Res* 42, 5217-5233.
- Chang, C.T., Muthukumar, S., Weber, R., Leviansky, Y., Chen, Y., Bhandari, D., Igreja, C., Wohlbald, L., Valkov, E., and Izaurralde, E. (2019). A low-complexity region in human XRN1 directly recruits deadenylation and decapping factors in 5'-3' messenger RNA decay. *Nucleic Acids Res* 47, 9282-9295.
- Chang, J.H., Jiao, X., Chiba, K., Oh, C., Martin, C.E., Kiledjian, M., and Tong, L. (2012). Dxo1 is a new type of eukaryotic enzyme with both decapping and 5'-3' exoribonuclease activity. *Nat Struct Mol Biol* 19, 1011-1017.
- Charenton, C., Taverniti, V., Gaudon-Plesse, C., Back, R., Séraphin, B., and Graille, M. (2016). Structure of the active form of Dcp1-Dcp2 decapping enzyme bound to m7GDP and its Edc3 activator. *Nat Struct Mol Biol* 23, 982-986.
- Chu, Q., Moellering, R., Hilinski, G., Kim, Y., Grossmann, T., Yeh, J., and Verdine, G. (2015). Towards understanding cell penetration by stapled peptides. *MedChemComm* 6, 111-119.
- Cohen, L.S., Mikhli, C., Jiao, X., Kiledjian, M., Kunkel, G., and Davis, R.E. (2005). Dcp2 Decaps m2,2,7GpppN-capped RNAs, and its activity is sequence and context dependent. *Mol Cell Biol* 25, 8779-8791.
- Courel, M., Clément, Y., Bossevain, C., Foretek, D., Vidal Cruchez, O., Yi, Z., Bénard, M., Benassy, M.N., Kress, M., Vindry, C., *et al.* (2019). GC content shapes mRNA storage and decay in human cells. *Elife* 8, e49708.
- Cox, J., and Mann, M. (2008). MaxQuant enables high peptide identification rates, individualized p.p.b.-range mass accuracies and proteome-wide protein quantification. *Nat Biotechnol* 26, 1367-1372.
- D'Lima, N.G., Ma, J., Winkler, L., Chu, Q., Loh, K.H., Corpuz, E.O., Budnik, B.A., Lykke-Andersen, J., Saghatelian, A., and Slavoff, S.A. (2017). A human microprotein that interacts with the mRNA decapping complex. *Nat Chem Biol* 13, 174-180.
- Dai, L., Zhao, T., Bisteau, X., Sun, W., Prabhu, N., Lim, Y.T., Sobota, R.M., Kaldis, P., and Nordlund, P. (2018). Modulation of Protein-Interaction States through the Cell Cycle. *Cell* 173, 1481-1494.e1413.
- Deyle, K., Kong, X.D., and Heinis, C. (2017). Phage Selection of Cyclic Peptides for Application in Research and Drug Development. *Acc Chem Res* 50, 1866-1874.
- Dietrich, L., Rathmer, B., Ewan, K., Bange, T., Heinrichs, S., Dale, T.C., Schade, D., and Grossmann, T.N. (2017). Cell Permeable Stapled Peptide Inhibitor of Wnt Signaling that Targets  $\beta$ -Catenin Protein-Protein Interactions. *Cell Chem Biol* 24, 958-968.e955.
- Dunckley, T., and Parker, R. (1999). The DCP2 protein is required for mRNA decapping in *Saccharomyces cerevisiae* and contains a functional MutT motif. *EMBO J* 18, 5411-5422.
- Eulalio, A., Behm-Ansmant, I., and Izaurralde, E. (2007). P bodies: at the crossroads of post-transcriptional pathways. *Nat Rev Mol Cell Biol* 8, 9-22.
- Fairhead, M., and Howarth, M. (2015). Site-specific biotinylation of purified proteins using BirA. *Methods Mol Biol* 1266, 171-184.
- Fenger-Gron, M., Fillman, C., Norrild, B., and Lykke-Andersen, J. (2005). Multiple processing body factors and the ARE binding protein TTP activate mRNA decapping. *Mol Cell* 20, 905-915.
- Grudzien-Nogalska, E., Jiao, X., Song, M.G., Hart, R.P., and Kiledjian, M. (2016). Nudt3 is an mRNA decapping enzyme that modulates cell migration. *RNA* 22, 773-781.
- Grudzien-Nogalska, E., and Kiledjian, M. (2017). New insights into decapping enzymes and selective mRNA decay. *Wiley Interdiscip Rev RNA* 8. DOI:10.1002/wrna.1379
- He, F., Celik, A., Wu, C., and Jacobson, A. (2018). General decapping activators target different subsets of inefficiently translated mRNAs. *Elife* 7.
- Heinis, C., Rutherford, T., Freund, S., and Winter, G. (2009). Phage-encoded combinatorial chemical libraries based on bicyclic peptides. *Nat Chem Biol* 5, 502-507.
- Horne, W.S., and Grossmann, T.N. (2020). Proteomimetics as protein-inspired scaffolds with defined tertiary folding patterns. *Nat Chem* 12, 331-337.
- Howarth, M., Takao, K., Hayashi, Y., and Ting, A.Y. (2005). Targeting quantum dots to surface proteins in living cells with biotin ligase. *Proc Natl Acad Sci U S A* 102, 7583-7588.
- Hubstenberger, A., Courel, M., Bénard, M., Souquere, S., Ernoul-Lange, M., Chouaib, R., Yi, Z., Morlot, J.B., Munier, A., Fradet, M., *et al.* (2017). P-Body Purification Reveals the Condensation of Repressed mRNA Regulons. *Mol Cell* 68, 144-157.e145.
- Jafari, R., Almqvist, H., Axelsson, H., Ignatushchenko, M., Lundbäck, T., Nordlund, P., and Martinez Molina, D. (2014). The cellular thermal shift assay for evaluating drug target interactions in cells. *Nat Protoc* 9, 2100-2122.
- Jiao, X., Chang, J.H., Kilic, T., Tong, L., and Kiledjian, M. (2013). A mammalian pre-mRNA 5' end capping quality control mechanism and an unexpected link of capping to pre-mRNA processing. *Mol Cell* 50, 104-115.
- Jiao, X., Doamekpor, S.K., Bird, J.G., Nickels, B.E., Tong, L., Hart, R.P., and Kiledjian, M. (2017). 5' End Nicotinamide Adenine Dinucleotide Cap in Human Cells Promotes RNA Decay through DXO-Mediated deNADding. *Cell* 168, 1015-1027.e1010.
- Jonas, S., and Izaurralde, E. (2013). The role of disordered protein regions in the assembly of decapping complexes and RNP granules. *Genes Dev* 27, 2628-2641.
- Kiledjian, M. (2018). Eukaryotic RNA 5'-End NAD(+) Capping and DeNADding. *Trends Cell Biol* 28, 454-464.
- LaRochelle, J.R., Cobb, G.B., Steinauer, A., Rhoades, E., and Schepartz, A. (2015). Fluorescence correlation spectroscopy reveals highly efficient cytosolic delivery of certain penta-arg proteins and stapled peptides. *J Am Chem Soc* 137, 2536-2541.
- Li, Y., Dai, J., Song, M., Fitzgerald-Bocarsly, P., and Kiledjian, M. (2012). Dcp2 decapping protein modulates mRNA stability of the critical interferon regulatory factor (IRF) IRF-7. *Mol Cell Biol* 32, 1164-1172.
- Li, Y., and Kiledjian, M. (2010). Regulation of mRNA decapping. *Wiley Interdiscip Rev RNA* 1, 253-265.
- Li, Y., Song, M., and Kiledjian, M. (2011). Differential utilization of decapping enzymes in mammalian mRNA decay pathways. *RNA* 17, 419-428.
- Li, Y., Song, M.G., and Kiledjian, M. (2008). Transcript-specific decapping and regulated stability by the human Dcp2 decapping protein. *Mol Cell Biol* 28, 939-948.
- Liu, S.W., Jiao, X., Welch, S., and Kiledjian, M. (2008). Analysis of mRNA decapping. *Methods Enzymol* 448, 3-21.
- Luo, Y., Na, Z., and Slavoff, S. (2018). P-Bodies: Composition, Properties, and Functions. *Biochemistry* 57, 2424-2431.

Luo, Y., Schofield, J., Simon, M.D., and Slavoff, S.A. (2020). Global profiling of cellular substrates of human Dcp2. *Biochemistry*. DOI: 10.1021/acs.biochem.0c00069

Lykke-Andersen, J. (2002). Identification of a human decapping complex associated with hUpf proteins in nonsense-mediated decay. *Mol Cell Biol* 22, 8114-8121.

Mugridge, J.S., Collier, J., and Gross, J.D. (2018a). Structural and molecular mechanisms for the control of eukaryotic 5'-3' mRNA decay. *Nat Struct Mol Biol* 25, 1077-1085.

Mugridge, J.S., Tibble, R.W., Ziemniak, M., Jemielity, J., and Gross, J.D. (2018b). Structure of the activated Edc1-Dcp1-Dcp2-Edc3 mRNA decapping complex with substrate analog poised for catalysis. *Nat Commun* 9, 1152.

Mugridge, J.S., Ziemniak, M., Jemielity, J., and Gross, J.D. (2016). Structural basis of mRNA-cap recognition by Dcp1-Dcp2. *Nat Struct Mol Biol* 23, 987-994.

Na, Z., Luo, Y., Schofield, J.A., Smelyansky, S., Khitun, A., Muthukumar, S., Valkov, E., Simon, M.D., and Slavoff, S.A. (2020). The NBDY Microprotein Regulates Cellular RNA Decapping. *Biochemistry*. DOI: 10.1021/acs.biochem.0c00672

Ng, S., Juang, Y.C., Chandramohan, A., Kaan, H.Y.K., Sadruddin, A., Yuen, T.Y., Ferrer-Gago, F.J., Lee, X.C., Liew, X., Johannes, C.W., *et al.* (2020). De-risking Drug Discovery of Intracellular Targeting Peptides: Screening Strategies to Eliminate False-Positive Hits. *ACS Med Chem Lett* 11, 1993-2001.

Nissan, T., and Parker, R. (2008). Analyzing P-bodies in *Saccharomyces cerevisiae*. *Methods Enzymol* 448, 507-520.

Paquette, D.R., Tibble, R.W., Daifuku, T.S., and Gross, J.D. (2018). Control of mRNA decapping by autoinhibition. *Nucleic Acids Res* 46, 6318-6329.

Perkins, D.N., Pappin, D.J., Creasy, D.M., and Cottrell, J.S. (1999). Probability-based protein identification by searching sequence databases using mass spectrometry data. *Electrophoresis* 20, 3551-3567.

Piccirillo, C., Khanna, R., and Kiledjian, M. (2003). Functional characterization of the mammalian mRNA decapping enzyme hDcp2. *RNA* 9, 1138-1147.

Rentero Rebollo, I., and Heinis, C. (2013). Phage selection of bicyclic peptides. *Methods* 60, 46-54.

Schatz, P.J. (1993). Use of peptide libraries to map the substrate specificity of a peptide-modifying enzyme: a 13 residue consensus peptide specifies biotinylation in *Escherichia coli*. *Biotechnology (N Y)* 11, 1138-1143.

Schindelin, J., Arganda-Carreras, I., Frise, E., Kaynig, V., Longair, M., Pietzsch, T., Preibisch, S., Rueden, C., Saalfeld, S., Schmid, B., *et al.* (2012). Fiji: an open-source platform for biological-image analysis. *Nat Methods* 9, 676-682.

Schmittgen, T.D., and Livak, K.J. (2008). Analyzing real-time PCR data by the comparative C(T) method. *Nat Protoc* 3, 1101-1108.

Schofield, J.A., Duffy, E.E., Kiefer, L., Sullivan, M.C., and Simon, M.D. (2018). TimeLapse-seq: adding a temporal dimension to RNA sequencing through nucleoside recoding. *Nat Methods* 15, 221-225.

She, M., Decker, C.J., Svergun, D.I., Round, A., Chen, N., Muhrad, D., Parker, R., and Song, H. (2008). Structural basis of dcp2 recognition and activation by dcp1. *Mol Cell* 29, 337-349.

Sheth, U., and Parker, R. (2003). Decapping and decay of messenger RNA occur in cytoplasmic processing bodies. *Science* 300, 805-808.

Song, M.G., Li, Y., and Kiledjian, M. (2010). Multiple mRNA decapping enzymes in mammalian cells. *Mol Cell* 40, 423-432.

Tan, C.S.H., Go, K.D., Bisteau, X., Dai, L., Yong, C.H., Prabhu, N., Ozturk, M.B., Lim, Y.T., Sreekumar, L., Lenggqvist, J., *et al.* (2018). Thermal proximity coaggregation for system-wide profiling of protein complex dynamics in cells. *Science* 359, 1170-1177.

Tritschler, F., Braun, J.E., Motz, C., Igreja, C., Haas, G., Truffault, V., Izaurralde, E., and Weichenrieder, O. (2009). DCP1 forms asymmetric trimers to assemble into active mRNA decapping complexes in metazoa. *Proc Natl Acad Sci U S A* 106, 21591-21596.

Tyanova, S., Temu, T., Sinitcyn, P., Carlson, A., Hein, M.Y., Geiger, T., Mann, M., and Cox, J. (2016). The Perseus computational platform for comprehensive analysis of (prote)omics data. *Nat Methods* 13, 731-740.

Valkov, E., Muthukumar, S., Chang, C.T., Jonas, S., Weichenrieder, O., and Izaurralde, E. (2016). Structure of the Dcp2-Dcp1 mRNA-decapping complex in the activated conformation. *Nat Struct Mol Biol* 23, 574-579.

Vinogradov, A.A., Yin, Y., and Suga, H. (2019). Macrocyclic Peptides as Drug Candidates: Recent Progress and Remaining Challenges. *J Am Chem Soc* 141, 4167-4181.

Walensky, L.D., and Bird, G.H. (2014). Hydrocarbon-stapled peptides: principles, practice, and progress. *J Med Chem* 57, 6275-6288.

Wang, X., Lu, Z., Gomez, A., Hon, G.C., Yue, Y., Han, D., Fu, Y., Parisien, M., Dai, Q., Jia, G., *et al.* (2014). N6-methyladenosine-dependent regulation of messenger RNA stability. *Nature* 505, 117-120.

Wang, Z., Jiao, X., Carr-Schmid, A., and Kiledjian, M. (2002). The hDcp2 protein is a mammalian mRNA decapping enzyme. *Proc Natl Acad Sci U S A* 99, 12663-12668.

Wurm, J.P., Holdermann, I., Overbeck, J.H., Mayer, P.H.O., and Sprangers, R. (2017). Changes in conformational equilibria regulate the activity of the Dcp2 decapping enzyme. *Proc Natl Acad Sci U S A* 114, 6034-6039.

Xu, J., Yang, J.Y., Niu, Q.W., and Chua, N.H. (2006). Arabidopsis DCP2, DCP1, and VARICOSE form a decapping complex required for postembryonic development. *Plant Cell* 18, 3386-3398.

Yoon, J.H., Choi, E.J., and Parker, R. (2010). Dcp2 phosphorylation by Ste20 modulates stress granule assembly and mRNA decay in *Saccharomyces cerevisiae*. *J Cell Biol* 189, 813-827.

Ziemniak, M., Mugridge, J.S., Kowalska, J., Rhoads, R.E., Gross, J.D., and Jemielity, J. (2016). Two-headed tetraphosphate cap analogs are inhibitors of the Dcp1/2 RNA decapping complex. *RNA* 22, 518-529.